ELM transient replication using pulsed plasma in Magnum-PSI

de Kruif, T.M.

Award date:
2013

ELM transient replication using pulsed plasmas in Magnum-PSI

Thijs de Kruif

Eindhoven University of Technology
Department of Applied Physics
Nuclear Fusion Group

Under supervision of:
Greg De Temmerman[1]
Niek Lopes Cardozo[2]

June 13, 2013

[1]FOM Institute DIFFER
[2]Eindhoven University of Technology

Abstract

Plasma-wall interactions are one of the major challenges for the next-generation fusion reactor, ITER. On top of the high steady-state plasma flux, transient events such as Edge-Localized Modes (ELMs) will cause regular transient heating of the surface, and are expected to reduce the lifetime of the divertor and the performance of the plasma. To assess the damage of ELMs on the wall material, a new experimental setup has been developed that can superimpose periodic high density heat and particle fluxes on a steady-state plasma flux by discharging a capacitor bank array through the source of the Magnum-PSI linear plasma device. In this thesis, this setup will be characterized and the response to tungsten targets due to pulsed plasmas on the surface will be presented.

The system was shown to dissipate 80% of the stored energy in the plasma, while resembling the pulse duration, approximately 1 ms, and shape as expected for an ELM in ITER. The peak electron temperature and density obtained during a pulse close to the target were 6.8 eV and 12×10^{20} m^{-3}, respectively. The peak heat flux on the target surface due to the transient increase of plasma parameters was found to be 180 MWm^{-2} with corresponding energy flux of 60 kJm^{-2}. Although the peak values are currently lower than the values expected for ITER-like ELMs, it is shown that with higher B-field the required conditions will be met. Through several experiments on tungsten targets, such as monoblocks designed for the ITER divertor, it is shown that the combined transient increase of both particle and heat flux will lead to different effects compared to other ELM replication experiments. The pulsed plasma system could therefore serve in the future as an important facility to test components planned for the ITER design.

Contents

Chapter 1

Introduction

1.1 Fusion energy

The world population is growing, the demand for energy is increasing, and the use of fossil fuels is likely affecting the climate. Therefore, the world is facing increasing problems to satisfy growing energy needs. Alternative energy sources are needed on a large scale and should be sustainable, clean and safe to provide a long-term solution to these energy problems while not harming our environment [1].

One promising candidate that can provide this energy over a sufficiently long time-scale (potentially $> 10^9$ years), in a safe and clean way is nuclear fusion [2]. Nuclear fusion is a process which involves the fusing of light elements resulting in excess energy. To achieve nuclear fusion in a self-sustaining way, sufficiently high temperatures, densities and confinement times of the fusing atoms are needed. Tokamaks are currently one of the best understood and most promising devices to satisfy these criteria and produce energy from fusion. The tokamak is a torus-shaped vacuum vessel surrounded by magnetic coils, as shown in figure 1.1, in which the fuel particles are ionized and heated to temperatures over 150 million degrees. The particles are magnetically confined along the axis of the torus (toroidal direction) through a toroidal current and external magnetic fields [3].

The first tokamak that is designed to generate more power than is needed to sustain these temperature (500 MW out for 50 MW in) for a relatively long duration (300-500 s) is ITER, which is currently being build in Cardache, France [4]. The design of ITER is shown in figure 1.2a. The project is an international collaboration and is planned to generate its first plasma in 2022 [5].

1.2 The challenge of Plasma Wall Interaction

The exhaust products in the form of heat and particles will need to be removed from the hot plasma, and therefore contact with the surface of the wall of the tokamak is unavoidable. The interaction of the fusion plasma with the plasma facing materials (PFMs), Plasma Wall Interaction (PWI), is one of the main issues in future generation tokamaks, due to the extremely high heat and particle fluxes [6]. In ITER, these fusion products are removed in the *divertor*, highlighted in figure 1.2a and shown in detail in figure 1.2b.

The divertor is positioned in the lower part of the toroidal wall. It hosts a region that is isolated from the core confined plasma, outside of the closed magnetic field lines. Plasma

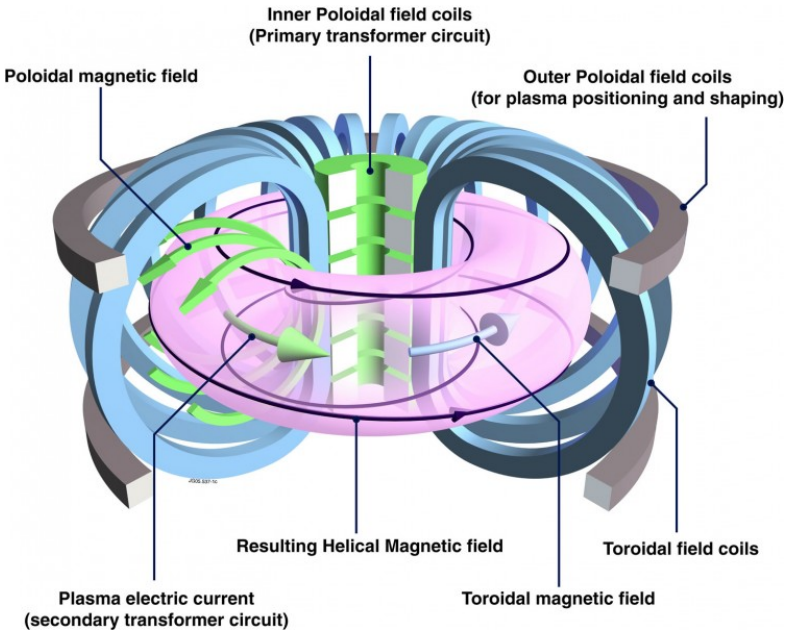

Figure 1.1: Basic design of a tokamak. A plasma is confined in the core of a torus by the helical magnetic field. The toroidal magnetic field is externally produced, while the poloidal magnetic field is generated through the toroidal plasma current. The current is induced by acting as the secondary winding in a transform circuit around the plasma vessel. (Source: EFDA-JET)

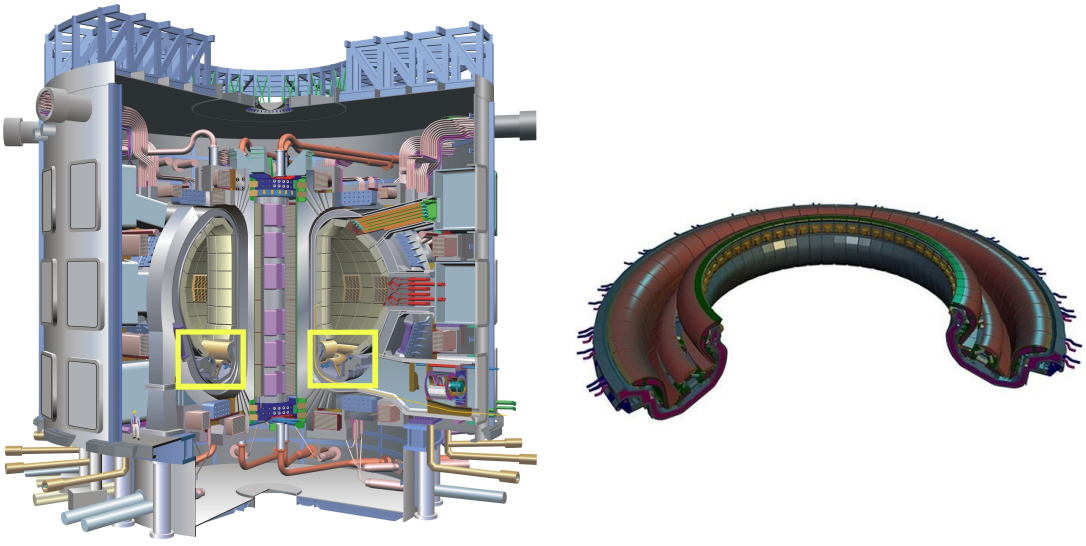

(a) (b)

Figure 1.2: (a) Design of the ITER tokamak. The position of the divertor is highlighted. (b) Design of the ITER divertor. The red plates are currently planned to be all-tungsten. (Source: ITER.org)

particles radially diffuse out of the confined region and will end up in the divertor. In steady-state operation, the expected heat fluxes in ITER are about 10 MWm^{-2} with particle fluxes of about 10^{24} $m^{-2}s^{-1}$ [7]. In these extreme conditions, PFMs could experience significant erosion processes such as melting and vaporization due to excess heat loads, and physical and chemical sputtering due to the high particle fluxes [8]. These processes have to be prevented or at least minimized as they greatly influence the performance and lifetime of the tokamak. For these reasons, tungsten is currently planned to be the material of the ITER divertor targets [4] as it has a high melting temperature, good thermal conducting properties, and low sputtering yield.

The more advanced tokamaks, such as ITER, are operated in a regime with steep pressure gradients between plasma and vacuum (H-mode) in which edge localized modes (ELMs) are triggered [9]. ELMs are periodic, short time-scale bursts of heat and particles from the main plasma to the divertor, leading to another concern regarding PWI in fusion reactors [10]. In ITER, type-I ELMs are predicted to reach energy densities of up to 10 MJm^{-2} during 1 ms with 1-10 Hz [11]. This will lead to strong transient temperature increases on the surface of the PFMs. The steep thermal gradients in the PFMs will induce thermal shocks that could result in cracks on the material surface [10]. The transient temperature excursions could furthermore cause the surface material to evaporate, or possibly melt a shallow region on the surface that could contaminate the plasma [6].

The effect of ELMs on PFMs is rarely being investigated in tokamaks [12, 13], because it is difficult to diagnose, understand, and predict the outcome of PWI processes in fusion reactors [14]. In JET, the largest present day tokamak, all wall material is replaced by the PFMs planned for ITER to address some of the issues expected regarding PWI [13]. Even in JET, however, ITER relevant exposure times and loads can not be reached. It is therefore essential to investigate the effect of ELMs on tungsten with a simultaneous steady-state plasma load in dedicated devices that can generate a controllable ITER-like environment. A better understanding of the behaviour of tungsten targets under these circumstances will greatly benefit the design of the divertor in ITER and future tokamaks as the expected effects can pose serious constraints on the lifetime of the reactor.

1.3 Steady-state and ELM simulations

To address the issues mentioned above, several dedicated ELM simulation experiments were set up such as the electron beam experiment in JUDITH [15], pulsed laser experiments in NAGDIS-II [16] and PISCES-A [17], and plasma guns (QSPAs) [18]. None of these experiments can, however, simulate both periodical heat and particles fluxes during a simultaneous steady-state plasma load which is expected for ELMs. The pulsed plasma system in Magnum-PSI is able to generate these conditions.

From the other ELM simulation experiments, nonetheless, interesting results were found. It was found that particles from a steady-state plasma modify the surface of a target which enhances the damage due to transient loading events when both are simultaneously present. Previously, this was observed at experiments combining pulsed lasers and steady-state linear plasma at the PISCES-A facility [19] and at NAGDIS-II [16]. In both experiments it was shown that the ablation threshold of tungsten was reduced when a simultaneous steady-state plasma was present, suggesting synergistic damage to the target. The pulsed laser experiments are still quite different compared to conditions expected in ITER, however. Although they do simulate the heat flux associated with an ITER-like ELM, they do not replicate the related particle flux [20]. In Pilot-PSI, a linear plasma generator at DIFFER, a cascaded arc plasma source is coupled to a capacitor bank. A discharge of the capacitor bank in the plasma source generates a high

density and temperature pulse superimposed on a steady-state plasma [21]. This enables the generation of ITER-like pulses with peak energy fluxes of $\sim$1 MJm^{-2} and pulse durations of $\sim$1.5 ms. In this setup the evaporation threshold found was lower compared to the pulsed laser simulations. It was suggested that the enhanced synergistic effects were caused by the presence of a transient particle source [20]. One of the drawbacks of this pulsed source, however, is its inability to generate periodic pulses, while in ITER periodic ELMs are expected.

To generate periodic pulses, a new system, based on the capacitor bank system, has been build to include multiple capacitor banks that can generate repetitive plasma pulses with a repetition rate of over 1000 Hz. The upgraded pulsed plasma system is installed in Magnum-PSI, which allows for better pumping of the vacuum vessel resulting in higher ion fluxes to the target. This setup allows, for the first time, for the investigation of the effects induced by combined ITER-like periodic transient particle and heat loads with steady-state plasma on a diverse range of targets. This unique setup could play an important role in testing the potential damage to the PFMs of the ITER divertor, currently one of the main challenges of the ITER design. The first ELM simulation experiments on actual tungsten monoblocks, that are currently proposed to be the main material for the ITER divertor, have already been started and initial results will be presented later in this thesis.

1.4 This thesis

The goal of this thesis is to investigate the effect of simultaneous steady-state plasma and periodic transient particle/heat fluxes on tungsten targets. The main research question to be investigated in this thesis is therefore:

What is the effect of periodic ITER-like ELMs with simultaneous steady-state plasma on tungsten targets?

To investigate this, this thesis will address three topics. Firstly, the performance of the pulsed plasma system will be investigated in chapter 3. The focus will mainly be on the relation between the input parameters and the resulting output plasma parameters. The operational range of the source will be discussed and the similarities between this setup and the setup in Pilot-PSI will be addressed. Secondly, the effect of plasma pulses on the target will be investigated in chapter 4. Here, the main focus is on the surface temperature and the heat flux evolution during and between pulses. In both chapters, the non-linear behaviour of the plasma when a target is present and the implications for the heat flux to the target will be discussed.

Finally, in chapter 5, the damage processes after pulsed plasma exposure are investigated for several types of tungsten targets both *in-situ* and *post-mortem*, amongst which the actual monoblocks which are expected to be installed in the divertor of ITER, . The results observed should give a better understanding of the damage mechanisms of transient events on tungsten targets. Here, an overview will be given of the results and implications for ITER on different targets used, such as fuzzy tungsten samples created in NAGDIS-II. Also the first results on the ITER monoblocks will be presented here which could serve as a first indication of the performance and life-time of the proposed ITER divertor. In more detail, the effects of shallow-melting of the surface of tungsten targets during ELMs will be investigated. The depth of the shallow-melt pool will be investigated here which could serve as a benchmark for similar melting experiments which are planned in JET in the summer of 2013.

Chapter 2

Experimental setup

The pulsed plasma system in Magnum-PSI consists of a capacitor bank array which can be discharged in parallel with a steady-state current through the plasma source of Magnum-PSI, thereby transiently increasing the produced plasma. In this chapter the background information associated with the setup of this experiments performed and the diagnostics used is described. First, Magnum-PSI, the Plasma-Wall testing facility at DIFFER, will be described in section 2.1. The basics of the cascaded arc plasma source will be explained and the operation of the device in non-pulsed mode will be discussed briefly. In section 2.2 the pulsed plasma system is described in more detail. This section will elaborate on the electrical components in the capacitor bank and the influence these components have on the expected power dissipation in the plasma. Finally, an overview and the technical specifications of the diagnostics used in this thesis will be given in 2.3. The non-trivial methods used in this thesis, specifically single-pulse Thomson scattering and the heat flux determination, will be described in more detail.

2.1 Magnum-PSI

Magnum-PSI consists of a cascaded arc plasma source connected to a cylindrical vacuum vessel. The generated plasma is confined by the longitudinal which guides the plasma to a retractable target. A schematic picture of this setup is shown in figure 2.1a.

A plasma is generated in the plasma source and driven into the vacuum vessel, as described in section 2.1.1. When the magnetic field coils are turned on, an axial magnetic field confines the plasma to a beam. The ions and electrons in this beam reach the target, located approximately 1 m downstream. Although Magnum-PSI is designed to be operated with a superconducting magnet, currently temporary copper coils magnet are installed. The coils limit the duration of the shot due to heating of the copper by the current. The sub-optimal geometry of these coils causes the magnetic field, furthermore, to diverge at the target position, leading to a broadening of the beam and a reduction of the axial B-field strength with a factor 5-7 at the target position. This is shown in figure 2.1b. The magnet can be operated in four settings, corresponding to the current in the copper coils. The B-field strength with corresponding settings is shown in table 2.1. The settings that is used usually depends on the nature of the experiment. Longer shot duration with lower magnetic field is a more time efficient method to obtain higher ion fluence to the target, while short shots with high heat flux are possible with high magnetic field. The latter is preferred for to maximize the heat flux during ELM simulations. In the remainder of the thesis, the B-field strength will be described with the setting number.

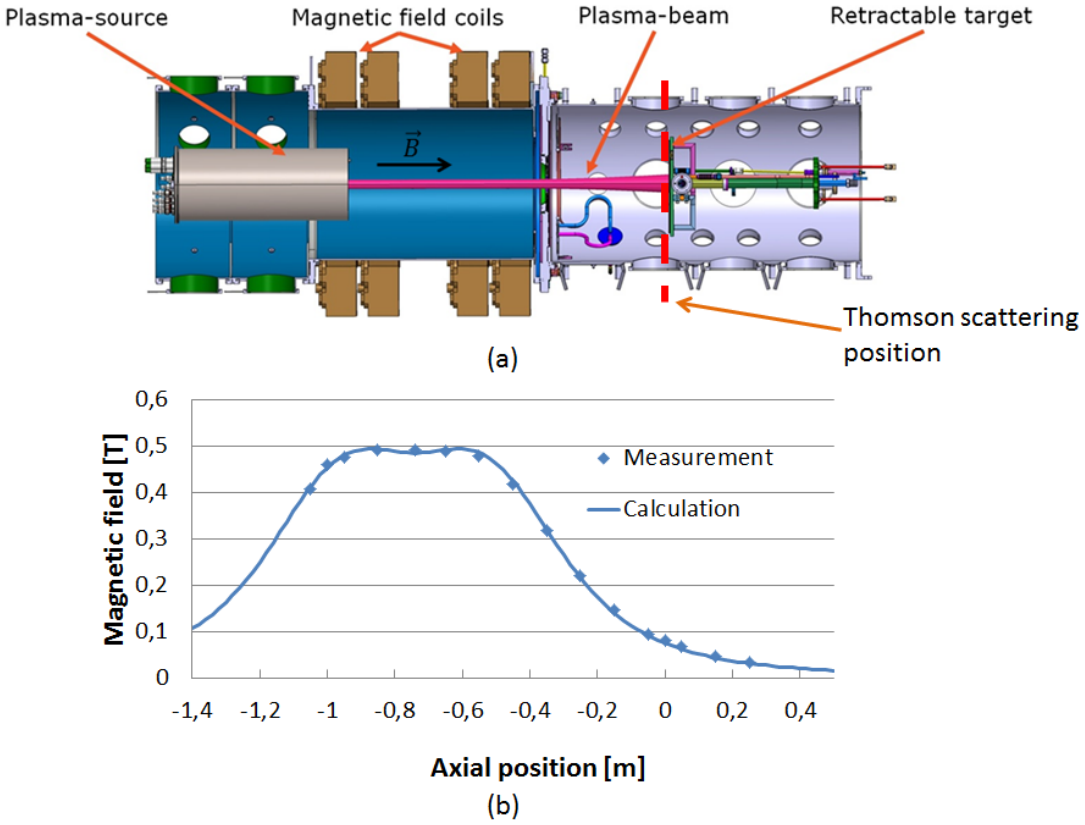

Figure 2.1: (a) Schematic overview of the Magnum-PSI facility at DIFFER. The system consists of a vacuum vessel surrounded with magnetic field coils. The plasma source and the retractable target are positioned along the direction of the axial magnetic field. (b) The simulated and measured axial magnetic field strength as a function of axial position (scaled with the design of Magnum-PSI as shown in (a)). Thomson scattering can be performed close to the target, where the axial position is at 0 m. Near the Thomson scattering position, outside of the magnetic field coils, the magnetic field is reduced due to the divergence of the field.

Table 2.1: An overview of the available B-field settings and the corresponding B-field strengths in Magnum-PSI. The B-field at the target position is the strength measured at the axial position where Thomson measurements are done. Most measurements were done at this position unless mentioned otherwise.

B-field setting	Current through coils (kA)	Linear B-field strength (T)	B-field strength at target position (T)	Maximal shot duration (s)
1	4.3	0.47	0.08	112
2	8.7	0.95	0.16	27.3
3	13.0	1.41	0.25	12.2
4	17,3	1.88	0.33	6.9

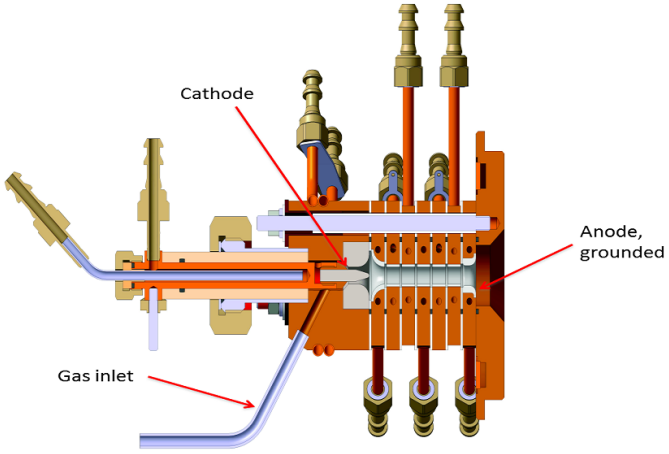

Figure 2.2: Schematic drawing of a typical cascaded arc plasma source used for pulsed plasma experiments. The model of the pulsed plasma source shown here contains a nozzle consisting of a copper plate with molybdenum inserts.

2.1.1 Cascaded arc plasma source

The cascaded arc plasma source, shown in figure 2.2, is the standard plasma source used in both Magnum-PSI and Pilot-PSI. It allows for the generation of high density plasmas with high particle fluxes and plasma temperatures in the eV range, similar to the divertor plasma expected in ITER.

The plasma source used to generate plasma pulses consists generally of six copper plates with molybdenum inserts with an inner diameter of ⌀10 mm. All of these plates are stacked together and insulated, using rubber O-rings and boron-nitride spacers, creating a arc plasma channel with each plate at floating potential. On one end, a lanthanum oxide-doped tungsten tip, the cathode, is connected and on the other end, a nozzle plate is installed, serving as the anode. The nozzle plate has an inner diameter of ⌀10.5 mm. Because the nozzle receives a large power flux and could deteriorate, several materials have been tested as inner materials during the experiment. For this thesis 1.5 mm thick Molybdenum inserts, full copper-tungsten (25%-75%) composite (Cu/W) nozzle plates, and tungsten coated (200 nm) Cu/W nozzle plates were used. All of the components are water-cooled to approximately 20°C.

Due to the high heat loads on the nozzle, impurities can be generated in the source due to melting or evaporation of the inner material. To monitor this, impurity lines in the plasma are measured using optical emission spectroscopy. The impurities most observed were mainly calcium and copper. The integration time (1.1 ms $< t_{Integration} <$ 10 s) of the spectrometer used here, OES1-Avantes, is however too long to accurately measure the impurity generation during a pulse.

Through a gas inlet on the cathode side, gas is injected into the plasma channel. Electrons are thermionically emitted from the cathode, leading to a high density plasma in the arc channel sustained by the current between cathode and anode [22]. The arc channel exhaust on the anode side is connected to a vacuum. The resulting pressure gradient between the gas inlet and the vacuum drives the plasma flow out of the arc channel into the vacuum vessel. In steady state operation the source is powered by a DC current-regulated power supply with currents ranging between 150 and 225 A. The gas used for this experiment was mainly H_2 with gas flows ranging

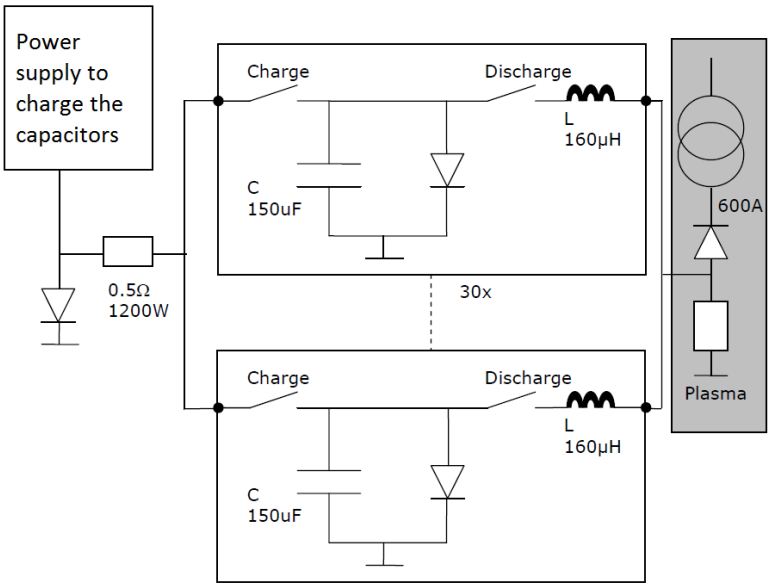

Figure 2.3: Schematic picture of the capacitor bank installed in Magnum-PSI. It consists of 30 parallel coupled sections that can be charged and discharged independently [25].

between 5.4 and 18 slm (Standard Liter per Minute) corresponding to arc channel pressures of 50 - 120 mbar, respectively.

2.2 Capacitor Bank

In 1984 it was shown by C.J. Timmermans that transiently increasing the current for a few milliseconds increases the electron density and electron temperature of the plasma produced by the cascaded arc source [23]. The setup, based on discharging a capacitor in parallel with the steady-state current, was replicated in a simplified form in Pilot-PSI for material testing under simultaneous continuous and transient plasma loads with an external magnetic field, as described extensively in the thesis of Jakub Zielinski [24]. This setup, consisting of 56 capacitors, is capable of discharging all capacitors at once, with a charging time of ∼10 s. To simulate type-I ELMs as foreseen in ITER, however, periodic plasma pulses are required. This feature is available on the capacitor bank system designed for Magnum-PSI.

A schematic picture of the electronic components in this setup is shown in figure 2.3. The system is divided into 30 sections. Each section consists of an inductor (160 μH), a capacitor (150 μF), charge and discharge switches which can be triggered externally, and an anti-reversal diode. When a capacitor is charged to the required voltage, the stored energy can be dissipated in a resistor, which in this case is the plasma. The resulting current pulse through the plasma is sustained during two modes, the resonance mode and the decay mode. In the resonance mode, the anti-reversal diode is non-conducting, forming an RLC circuit. The resulting current curve can be described by the first quarter of a sine wave,

$$I(t) = I_0 \sin(\frac{t}{\sqrt{LC}}) \quad \text{for } 0 < t < \frac{\pi}{2}\sqrt{LC}, \tag{2.1}$$

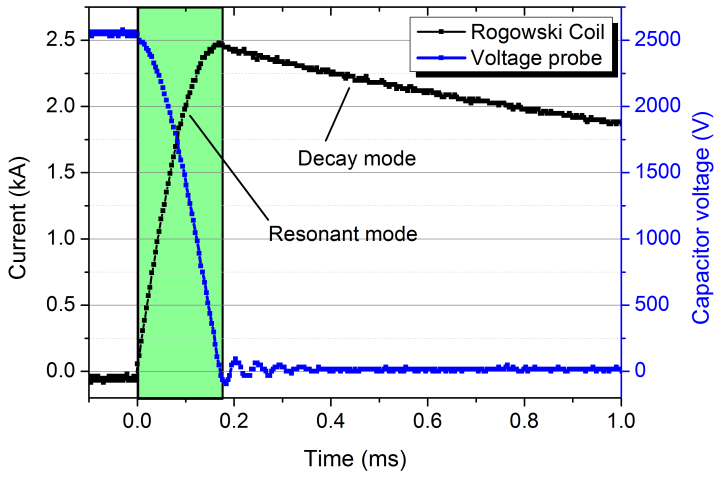

Figure 2.4: Typical current trace and capacitor voltage trace during a discharge on a dummy resistor (10 mOhm). During the pulse two regions can be distinguished. The resonance mode (green), when the charge in the capacitor is discharged, and the decay mode, when the voltage across the capacitor is zero, making a LR circuit.

where I_0 is the peak current of the system and L and C the characteristic inductance and capacitance, respectively.

The decay mode can be derived as (2.2). Its onset occurs when the current through the resistance is at its maximum and the voltage over the capacitors is zero. At this point, the anti-reversal diode becomes conducting and the section functions as an LR circuit. The resulting current through the plasma source will then become

$$I(t) = I_0 \exp^{-\frac{Rt}{L}} \quad \text{for } t > \frac{\pi}{2}\sqrt{LC}, \tag{2.2}$$

where R is the resistance of the plasma.

A typical current trace over a constant 10 mOhm resistance is shown in figure 2.4. Because all capacitors can be discharged independently, the pulse shape can be controlled by varying the delay time between the discharges of different capacitors. Alternatively, the total energy during a pulse can be increased by discharging several capacitor banks simultaneously. The total stored energy that is dissipated in one pulse is given by,

$$E_{Stored} = \frac{1}{2} n C V_{Charge}^2, \tag{2.3}$$

where n is the number of capacitors discharged in one pulse and V_{Charge} is the charging voltage of the capacitors. This allows the pulse to have different pulse lengths and a wide range of energies. Because the maximum charging voltage of one capacitor is 3000 V, theoretically the largest possible stored pulse energy is ∼20 kJ. The charging time of one section is approximately 22.2 ms and the maximum pulse frequency that can be obtained, when using one capacitor per pulse and alternating between all of capacitor banks, is 30×45=1350 Hz.

In the remainder of this thesis, a plasma *shot* is defined as the period between the magnetic field switching on and the magnetic field switching down. A plasma *pulse* is defined as

the discharge of the capacitor storing the pulse energy. This will lead to a plasma *pulse* with simultaneous steady-state plasma which is generated throughout the *shot*.

2.3 Diagnostics

For the analysis of the Magnum-PSI plasma, there are three regions of interest: The current/voltage characteristics in the source, the plasma evolution in the plasma beam, and the response of the target to the incoming plasma.

The voltage between cathode and anode was measured using a voltage probe, Yokogawa 100 MHZ 1400V Differential Probe, near the source. The current generated during a discharge was measured with a Rogowski coil, home-made at DIFFER, around the wires connecting the capacitor bank to the source. Both parameters were measured with high frequency ($\sim$100 kHz) to accurately investigate the evolution of the parameters during the millisecond pulse. Knowing these parameters, one can also determine the resistance of and the power dissipated in the plasma during the pulse.

Single-shot Thomson Scattering was used to measure the evolution of electron density and electron temperature evolution during a pulse. This is described in more detail in section 2.3.1.

The target is cooled using pressurised cooling water at $\sim$20°C. The power deposited on the target by the plasma is measured using calorimetry on the cooling water. In the pulsed plasma experiments, however, the energy added by the pulse is negligible compared to the integrated steady-state heat load and therefore the heat added by a pulse cannot be measured accurately. To measure the heat flux to the target during a transient event, a fast Infra-red (IR) Camera is used to measure the surface temperature. The temperature evolution is used as an input for the THEODOR code[26], which converts temperature to heat flux absorbed by the target surface. The fast IR-Camera and THEODOR are described in more detail in section 2.3.2. This method depends however on the emissivity of the target. Although the temperature dependent emissivity has been calibrated for polished tungsten targets, it is often unknown for other materials and surface morphologies. The emissivity can be determined by cross-correlating the data from the IR-Camera with the data obtained by a pyrometer on the target. The pyrometer, FAR SpectroPyrometer model FMPI, is able to eliminate the emissivity by looking at the ratio between multiple wavelengths in the IR-spectrum. Because the maximum sample rate of the pyrometer is 15 Hz, transient events cannot be measured. Finally, a fast visible camera, Phantom V12 Camera, is used to measure light in the visible spectrum at high speed ($>$ 10kHz). It is used to measure specific emission lines in the plasma beam or to measure morphology changes of the target.

For the *post-mortem* analysis of the exposed targets, optical microscopy was used to see the evolution of the grain structure of the tungsten targets. To look at the nano-structures and the surface morphology in more detail, scanning electron microscopy (SEM) was used. SEM was also used to investigate the cross-section of tungsten targets to analyse the depth of morphology changes. SEM analysis on the tungsten targets exposed during the experiments was done by the Department of Materials Engineering at the Institute of Plasma Physics, Czech.

2.3.1 Single-pulse Thomson scattering

The diagnostic used in Magnum-PSI to monitor the plasma conditions is incoherent Thomson scattering (TS) [27]. This system allows for measurements of the evolution of electron density, n_e, and electron temperature, T_e, in the plasma beam during the plasma pulse. The TS-system consists of a pulsed laser penetrating the plasma beam radially. The photons of the laser pulse are elastically scattered by the free electrons in a random direction. An array of optical fibres

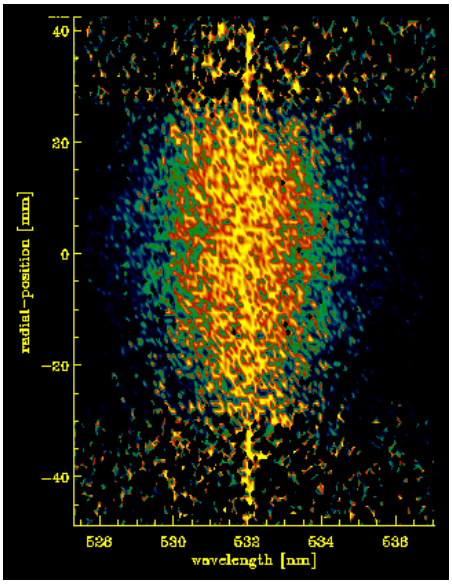

Figure 2.5: A typical image that the ICCD camera of the Thomson scattering system records during measurement of a plasma pulse. On the y-axis the radial profile is depicted which was measured by the array of optical fibres collecting light from different radial positions of the beam. On the x-axis the spectrum of collected light is depicted. This image can be converted to a radial profile of n_e and T_e.

that is measuring perpendicularly to the laser direction and the plasma beam axis, collects part of the scattered photons. The photons are diffracted in an optical grating and the resulting spectrum is recorded with an ICCD camera. The collected number of photons and the width of the measured spectrum can be used to determine n_e and T_e, respectively. As an example, the image projected on the ICCD camera is shown in figure 2.5.

The laser used in Magnum-PSI is a Nd:YAG laser operating in the second harmonic at 532 nm, with an repetition rate of approximately 8 Hz. The pulse duration is 10 ns (FWHM), with 0.7 J/pulse in pulse energy. With the current magnetic configuration in Magnum-PSI it is possible to do TS measurement in the beam at approximately 1 m downstream of the plasma source, near the target. The relative error in measured density due the spectrometer can be derived as,

$$\frac{\Delta n_e}{n_e} = \frac{1}{\sqrt{N_{pe}}}, \tag{2.4}$$

where N_{pe} are the generated photoelectrons in the photon-multiplier. The relative error in T_e is two times larger, $2N_{pe}^{-0.5}$ [28]. Because the electron density during a pulse is relatively high, single-pulse Thomson scattering can be performed with good accuracy. The relative errors for n_e and T_e were found to be $\sim$3% and $\sim$6% for $n_e > 2.8 \times 10^{20}\ m^{-3}$, respectively.

Because the integration time of the detection system is relatively short, 25 ns, it is possible to measure the plasma parameters during a plasma pulse. Both the capacitor bank and the TS laser can be triggered externally. With a 8 Hz pulse generator, it is possible to trigger both systems simultaneously to ensure the TS pulse is arriving in the plasma beam during a plasma pulse. By increasing the delay between both triggers, it is possible to measure the plasma parameters on a selected temporal interval during the $\sim$1 ms pulse. In this way it is possible to determine

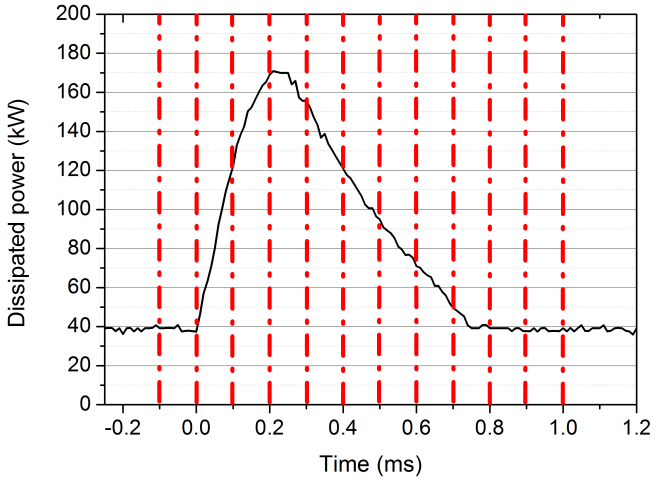

Figure 2.6: Typical power trace of a pulse with 60 J of stored energy. The moment of measurement with Thomson scattering (red lines) is controlled by the delay between trigger to the capacitor bank and Thomson laser. Here, measurements start 100 μs before the start of the pulse and the delay is increased with 100 μs steps for 11 pulses.

the spatial and temporal evolution of the plasma parameters during a pulse by systematically increasing this delay for each pulse and adding the measurement data. This is schematically shown in figure 2.6.

2.3.2 Determining the heat flux to the target

The surface temperature evolution during a plasma pulse is of importance when assessing the energy arriving at the target surface. The diagnostic used in Magnum-PSI is a fast IR-Camera because of the good spatial and temporal evolution. The camera used for these experiments, FLIR SC7500MB, can measure with rates up to 10 kHz, depending on the integration time and read-out time. The integration time for one frame during the experiments ranges between 10-200 μs which is sufficiently short to measure the temperature evolution during a plasma pulse. A typical image obtained with the IR-Camera of an ITER-monoblock during plasma exposure is shown in figure 2.7. The two parameters that need to be taken into account when converting the raw camera data to temperature are emissivity and transmission. Transmission is typically 90% in Magnum-PSI. The temperature dependent emissivity for polished tungsten has been measured for 27-3327 °C. For other surfaces the emissivity has to be determined from the pyrometer.

The measured 2D time evolution of the surface temperature is used as an input for a numerical calculation to find the heat flux, taking into account the temperature dependent material parameters, using the THEODOR code [29]. The heat fluxes are derived by numerically solving the bulk target temperature time evolution using,

$$\rho_W(T_{bulk})C_W(T_{bulk})\frac{\mathrm{d}T_{bulk}}{\mathrm{d}t} = \nabla q_{bulk}, \tag{2.5}$$

where ρ_W and C_W are the density and heat capacity of tungsten, respectively, and q_{bulk} is the heat flux to the bulk of the target. To prevent the code from calculating negative heat fluxes at

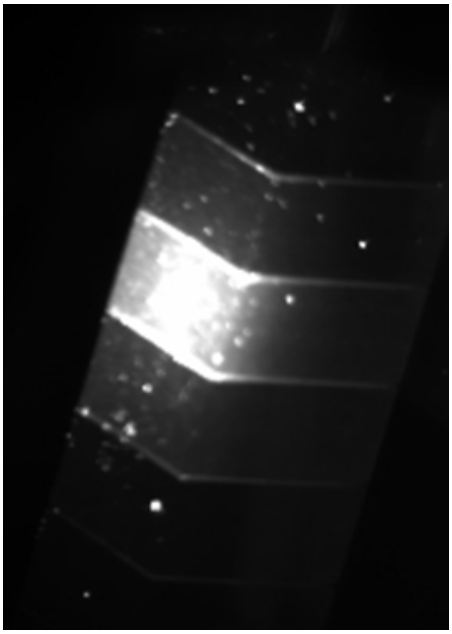

Figure 2.7: A typical image obtain with the IR-Camera during plasma exposure. In this case, a tungsten tile of an ITER monoblock is exposed in Magnum-PSI.

the end of a plasma pulse, which would imply active cooling of the surface, a thin layer on top of the surface is assumed that adds a decrease of heat conductivity because of the direct impact of the plasma pulse. The heat flux boundary conditions are determined by two parameters, α_{bottom} and α_{top}, describing the rear/lateral boundary conditions and front surface boundary conditions, respectively, according to,

$$q_{rear/lateral} = \alpha_{bottom}(T_{bulk} - T_{vessel}) \tag{2.6}$$

and

$$q_{front} = \alpha_{top}(T_{surf} - T_{bulk}). \tag{2.7}$$

The value for α_{bottom} was determined as 250 $\mathrm{kWm^{-2}K^{-1}}$, and the value α_{top} can be determined by varying the value and eliminating the calculated negative heat flux after the plasma pulse [26]. It was found that for measurements near the position of Thomson scattering, in the expanding B-field region, $\alpha_{top} \approx 1.5 \times 10^6$ $\mathrm{Wm^{-2}K^{-1}}$. For measurements in Pilot-PSI or when the target was further inserted into the linear B-field, as was the case for the ITER monoblocks, $\alpha_{top} > 5.0 \times 10^{10}$ $\mathrm{Wm^{-2}K^{-1}}$ was found.

Chapter 3

Characterization of the plasma pulse

To assess the effect of a capacitor discharge on the behaviour of the generated plasma, the pulsed system needs to be characterized. The response of the plasma pulse for different input parameters will be investigated and the subsequent operational space will be determined.

This chapter will look at three aspects. First, the effect of different pulse energies in the pulsed plasma system will be investigated in section 3.1. The output of these parameters in terms of power dissipation will be analysed according to the measured voltage and current evolution at the source. The response of the input parameters on the output will be discussed by looking at the role of resistance and inductance in the plasma. This should give a better understanding and allow for better control of the shape and peak values of the power evolution during a pulse. Second, the evolution of plasma parameters in the plasma beam as obtained from single-pulse Thomson scattering will be shown in section 3.2. From this section the operational range of the generated plasma parameters will be investigated. The relation between the power dissipated and the evolution of the plasma parameters will be discussed here, as well as the role of the source to the plasma output. Finally, the presence of the target in the pulsed plasma system will be investigated. In Magnum-PSI it is possible to retract the target, increasing the axial length of the plasma beam. The results of this experiment are discussed in section 3.3. An understanding of the plasma parameters close to the target will lead to a better understanding of the temperature response and surface modification processes due to pulsed plasmas that will be presented in the subsequent chapters.

3.1 The effect of the discharge of power dissipation in the plasma

3.1.1 Experimental methods

In this section, the power dissipated in the plasma during a plasma pulse will be investigated. The time evolution of dissipated power in the plasma will be analysed from the shape of the pulse and the peak dissipated power values. Furthermore, the response of the latter two parameters to changing pulse energy will be analysed. The pulse energy can be controlled by changing the stored energy in the capacitor bank, which can be done by varying the charging voltage of the capacitors in the capacitor bank and the amount of capacitors discharged in a pulse according to equation (2.3). Knowing the response of the dissipated power in the plasma for different pulse energies will allow for better control and a better understanding of the generation of plasma pulses in Magnum-PSI.

To do this, the plasma will be treated as an electric component in the pulsed plasma circuit.

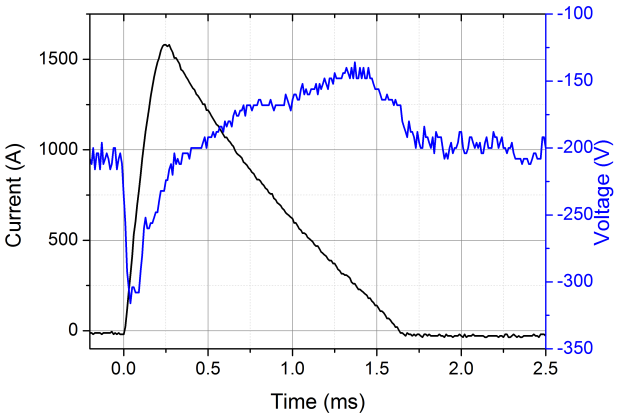

Figure 3.1: This figure shows a typical current and voltage trace during a capacitor discharge with 320 J stored energy in the plasma. The current was measured from the capacitor bank, not taking the DC-current into account. The voltage was measured between the cathode and the grounded anode of the plasma source. When the discharge switch is closed, the current through the plasma increases in 250 μs to 1.6 kA in resonance mode. When the voltage across the capacitors is zero, the pulsed plasma circuit switches to decay mode, where the current decays exponentially to zero with a decay time of 600 μs.

By analysing the impedance of the plasma during a pulse, the shape and peak values of the dissipated power can be understood. This is done by measuring the time evolution of current and voltage during a pulse in Magnum-PSI with simultaneous steady-state plasma and with the magnetic field switched on. The current evolution during a discharge and the voltage between cathode and anode of the source can be measured using a Rogowski coil and a voltage probe, respectively.

3.1.2 Results

A typical time trace of these parameters is shown in figure 3.1. Here, a single capacitor charged to 2066 V is storing 320 J energy. In steady-state, a DC current of 190 A sustains a hydrogen plasma resulting in a voltage difference of ~ -200 V in the source. When the capacitor is discharged at $t = 0$, the pulse current is superimposed on the DC-current in the source and rises in $\sim$250 μs to 1.6 kA. When the voltage difference across the capacitor plates is zero, the power dissipation changes from resonance mode to decay mode. The RLC-circuit becomes a RL-circuit and the superimposed current decays exponentially to zero with a e^{-1}-time of $\sim$600 μs.

Knowing the voltage and current, one can derive the dissipated power in the plasma, shown in figure 3.2 for different pulse energies stored in the capacitors. In this graph, two things can be observed that will be explored next in more detail. First, the peak power dissipated in the source increases from 140 to 380 kW with stored pulse energy increasing from 60 to 320 J in the resonance mode, and second, the pulse duration is increased by an increasing decay time from 300 to 600 μs in the decay mode.

The total energy dissipated in the plasma can be calculated by integrating the power evolution over time during the discharge. An overview of the total energy dissipated, $E_{Dissipated}$, for several experiments is shown in figure 3.3. The graph shows an approximately linear behaviour from

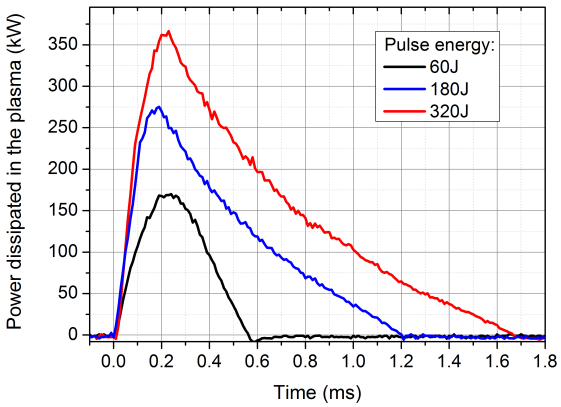

Figure 3.2: The time evolution of power dissipated in the plasma due to Ohmic heating during a discharge of capacitor. The capacitor discharges shown here were from a single section with V_{Charge} = 900 V (black), 1550 V (blue), and 2066 V (red). The shape of the power evolution resembles the expected shape of the heat flux evolution during an ELM in a divertor [30].

which the efficiency of the pulsed plasma source can be obtained. The fit shown in the graph gives an efficiency, $\eta = \frac{E_{Dissipated}}{E_{Stored}}$, of 80.1±0.7%. The remainder of the power is dissipated in the cables connecting the pulsed plasma system with the source and in the other electrical components of the capacitor bank (the diode, inductor and switches).

The peak power values measured for different pulse energies are shown in figure 3.4. For the pulse energies used in the experiments, the peak power is shown to increase from 50 kW to approximately 280 kW for energies from 30 J to 320 J. A non-linear relationship between pulse energy and peak power can be observed, however. To understand the peak power that can be dissipated, this relationship should be understood. Because most of the power is dissipated in the source due to Ohmic heating of the electrons, the resistance of the plasma influences the peak power. As will be shown later, the resistance decreases with electron temperature. Due to the lower resistance, the energy transfer efficiency in the plasma will decrease with increasing pulse energy, hence leading to less power dissipated in the plasma.

That resistance is the parameter determining the peak power dissipated in the source is indeed observed as shown in figure 3.5. The resistance is calculated by dividing the voltage by current. The resistance is minimal in Magnum-PSI when the current is maximal, at the moment of transition between resonance mode and decay mode. The measured resistance of the plasma ranges between 0.05 Ω during a pulse and 1.1 Ω in steady-state operation (DC). The fit inserted in the graph shows the dependency of the plasma conductance (R^{-1}_{Plasma}) to the peak current. A linear relationship between peak current and conductance is observed, where $R_{Plasma} \approx 263 I^{-1}_{peak}$. This can be explained from theory. When the current in the source is at its maximum, the charge over the capacitor is zero and therefore the voltage between cathode and anode is equal to the voltage during DC current. If the voltage between cathode and anode is constant, one would expect that $R_{Plasma} \propto I^{-1}$ according to Ohm's law. This implies that the resistance of the plasma is driving the peak power in the plasma regardless of the charging voltage of, and thus the stored energy in, the capacitors. The resistance, as will be shown later, is however influenced by the power dissipated in the plasma which does depend on the stored energy.

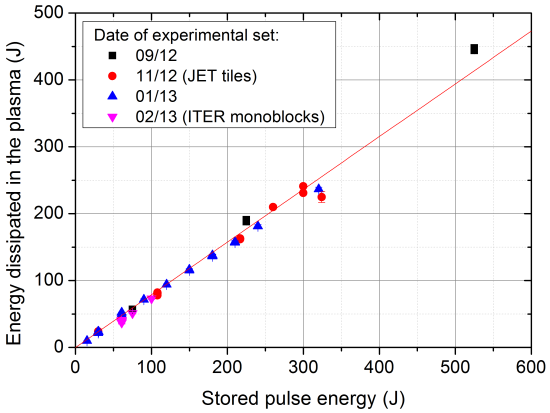

Figure 3.3: Total energy dissipated in the plasma during a plasma pulse. The dissipated energy, gathered from several experiments, was calculated from the time integrated power dissipation in the plasma. A linear fit was made to find the energy conversion efficiency of the pulsed plasma system. It shows that the efficiency is 80.1% compared to ∼50% in Pilot-PSI. The error bars shown here are an indication of the variance of values obtained for different pulses. In the remaining graphs in this section, showing peak values calculated from a set of pulses, the error bar is derived from the variable peak values found.

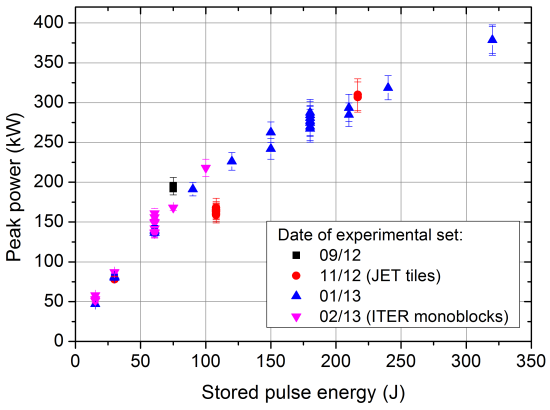

Figure 3.4: Peak power with stored pulse energy from several experiments. The peak power is defined as the maximum dissipated power during a pulse. Here, one capacitor was discharged for one pulse while only the charging voltage of the capacitor was varied. For all pulses, B-field setting 3 was applied. The peak power increases linear with stored pulse energy until $E_{stored} \approx 100$ J. For higher pulse energy, the increase with pulse energy is lower. This is probably caused by the decreasing plasma resistance.

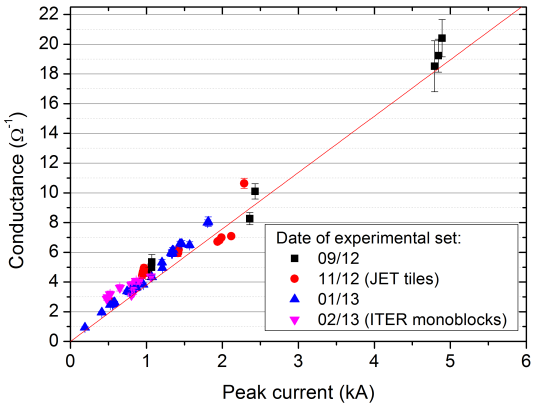

Figure 3.5: Graph showing the dependence of conductance on the peak current for several pulse energies. The conductance (current divided by voltage) shown here was taken at the moment of transition between resonance mode and decay mode. A linear relation between the current and conductance for several data sets was found.

A decrease of resistance in the plasma will also result in an increase in the pulse decay time according to equation (2.2). To see whether the values measured compare to what is expected from theory, the impedance of the other electrical components in the system needs to be investigated. This was done by performing similar experiments on a dummy resistance (10 mΩ and zero inductance). From this analysis an additional impedance from the wires to the source was found; a resistance $R_{Wire} = 48 \pm 10$ mΩ and an inductance $L_{Wire} = 24 \pm 14$ μH. The analysis of the dummy data is described in greater detail in appendix B. The total impedance of the pulsed plasma system is therefore $R_{Total} \approx 48\ m\Omega + R_{Plasma}$ and $L_{Total} \approx 184$ μH when using a single section per pulse. Both resistance and inductance are decreased when multiple sections are discharged in one shot. The decay time, τ_{decay}, for n sections discharged during a pulse can then be derived as,

$$\tau_{decay} = \frac{L_{tot}}{R_{tot}} = \frac{L_{Wire} + L_{Section}}{nR_{plasma} + R_{Wire}}. \tag{3.1}$$

An increase in the decay time with increasing plasma resistance is indeed observed as shown in figure 3.6. A power fit through the data shows that $\tau_{decay} \approx 102 \times 10^{-6} R_{total}^{-1.02\pm0.02}$. This inverse proportionality of the decay time with the total resistance is expected from the electronic characteristics. The value, 102 μH, found for the total inductance is lower then 184 μH, however. The lower value could be explained by the changing resistance throughout the pulse. When the power heating the plasma in the source decays exponentially, the resistance increases as shown in the inset of figure 3.6. The actual decay time of the pulse is therefore shorter due to the time-dependent impedance of the plasma.

So the resistivity in the plasma is changing due to Ohmic heating in the plasma. The electron transport in the plasma beam is dominated by electron conductivity when a magnetic field is present. The electron conductivity in a highly ionized gas, as is the case during a plasma pulse, is given by the Spitzer resistivity, η_e, which for hydrogen is [31]

$$\eta_e = 1 \times 10^4 (kT_e)^{-3/2} \ln \Lambda, \tag{3.2}$$

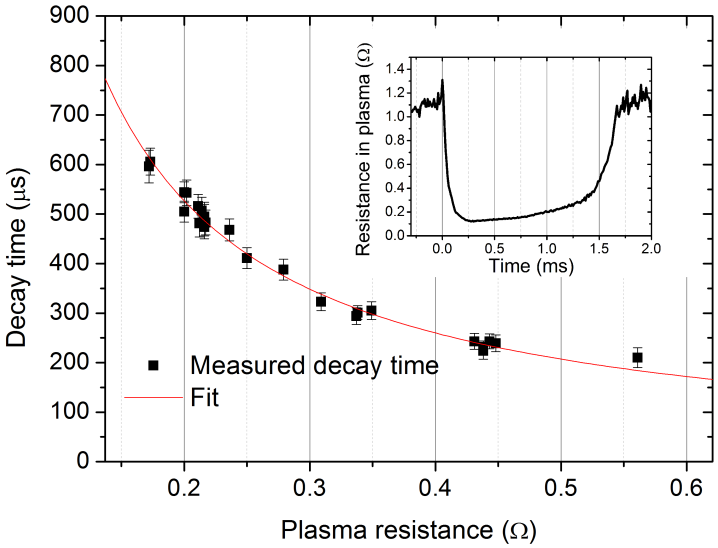

Figure 3.6: Graph showing how the decay time is influenced by the changing impedance of the plasma. The decay time is defined as the characteristic e^{-1}-time of the current in decay mode and the plasma resistance is taken at the moment of transition between resonance mode and decay mode. The decay time of the current evolution is shown to scale inversely with the plasma resistance as is expected from equation (3.1). Inset: The typical evolution of the plasma resistance during a 320 J pulse. The resistance is increasing with time in decay mode which decreases the decay time of the pulse.

where T_e is the electron temperature and $\ln \Lambda$ is the Coulombic logarithm with a typical value of approximately 7, found for Pilot-PSI [32]. The total resistance scales as

$$R_{plasma} \propto \eta_e \ell, \tag{3.3}$$

where ℓ is the length of the current path. An increase of the electron temperature along the current path of the electrons therefore decreases the resistance during a plasma pulse which controls the peak power dissipated in the source and the decay time of the plasma pulse.

3.1.3 Conclusions and discussion

In the previous section, the impedance of the plasma was investigated during a plasma pulse to allow for better control of the dissipated power in the plasma during a plasma pulse. This was done from the results obtained of the I-V characteristics of the pulsed plasma system. The typical peak values of dissipated power, ranging from 140 to 380 kW, have been shown as well as the characteristics of the shape of the pulse. It was shown that ∼80% of the stored energy in the capacitor bank is dissipated in the plasma due to Ohmic heating. The non-linear behaviour of the peak power and the increasing decay time of the pulse with increasing pulse energy both indicate that the resistance in the source is lowered during a plasma pulse, which indicates an increase of the electron temperature due to Ohmic heating.

Although the plasma could also have a time-dependent inductance during a transient event, this could not be observed from the measurements presented here. This is mainly due to the large error in determining the characteristic ramp up and decay time of the pulse, due to fluctuations in the voltage measurements, and the changing resistance over time. If there were inductive effects present, they do not seem to affect the pulse shape significantly compared to the changing resistance.

To see whether the response of the plasma to a discharge of capacitors in Magnum-PSI is similar to the response to pulses in Pilot-PSI, the plasma resistance as a function of dissipated energy is compared. The plasma resistance as a function of the dissipated energy in the plasma for both systems is shown in figure 3.7. Also a decrease of the Spitzer resistivity is observed in Pilot-PSI. In Pilot it is also possible to measure the electron temperature 4 cm away from the source, which also shows an increase in T_e for decreasing resistance. Assuming that this is also the case for Magnum-PSI close to the source, this would confirm that Spitzer resistivity is decreasing with increasing pulse energy. The electronic design of the capacitor bank in Pilot does differ, however, from the electronic design in the capacitor bank of Magnum-PSI. Because in Pilot the voltage across the capacitors can become both positive and negative, the system will be in resonance mode during the full pulse whereas the capacitor bank in Magnum will switch to decay mode when the voltage across the capacitors is zero. Therefore, the pulse shape between the two systems is quite different. The electronic differences between the two systems and the corresponding I-V characteristics are investigated more thoroughly in appendix A.

The resistance due to a plasma pulse with similar dissipated energy and pulse length is observed to be almost a factor 2 lower in Pilot-PSI compared to Magnum, as shown in figure 3.7. There are two factors that could explain the lower resistance. First, the current path in Pilot is presumably shorter (∼0.5 m from source to target) compared to Magnum (∼1 m from source to target). As the majority of the electron current is driven in the plasma beam when the magnetic field is on, the current path of the electrons is 'shorted' when arriving at the conducting target. This should, according to equation 3.3, reduce the total resistance and increase the power dissipated in the plasma. It is assumed that the majority of the electrons in Pilot-PSI are shorted by the target [33]. But, as will be discussed in section 3.3, it is not sure how much of the electron current actually arrives at the target in Magnum-PSI. Second, the electron temperature in the

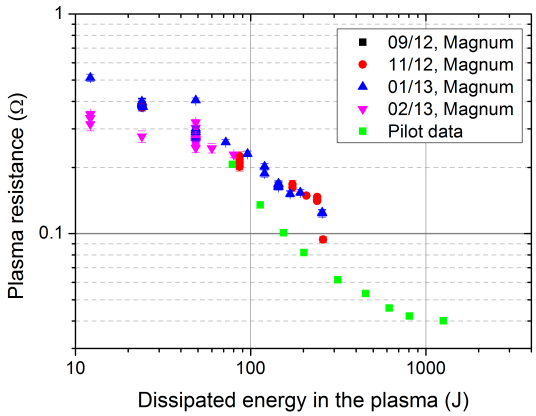

Figure 3.7: Comparison between the plasma resistance in Pilot-PSI and Magnum-PSI. For the Pilot-PSI data [24], the dissipated energy and plasma resistance were calculated in a similar way as for Magnum-PSI. The resistance was shown to be lower in Pilot-PSI for similar dissipated energy.

beam could be lower in Magnum. As the B-field in Pilot-PSI is generally higher, the resistance is higher and more power can be dissipated in the plasma. This is not significant within the straight magnetic field, where the B-field strength is similar. Close to the target, however, where the magnetic field is expanding and axial magnetic field strength is lower, the electron temperature could decrease significantly.

Either way, this shows that the plasma resistance is generally higher in Magnum. With the current magnet configuration it is therefore likely that a smaller part of the electron current will reach the target.

3.2 Evolution of the plasma parameters during a pulse

3.2.1 Experimental method

Now that the response of a capacitor discharge in the plasma beam as part of the electronic circuit has been investigated, the plasma parameters as a results of the plasma pulse are addressed next. In this section two questions will be answered: *How do plasma parameters change with power dissipated in the plasma due to Ohmic heating?* and *For what pulse energies can the optimal heat and particle flux to the target be achieved?*. This will allow us to know the range of plasma parameters that can be generated during a plasma pulse and will lead to a better control of input parameters to obtain the required plasma parameters.

In the current configuration of Magnum-PSI, it is possible to measure the electron density and electron temperature in the plasma beam by single-shot Thomson Scattering near the target, ∼1 m downstream of the source, as explained in more detail in section 2.3.1. By changing the delay between the trigger of the Nd-YAG pulsed laser and the capacitor bank, the plasma parameters during different stages of the plasma pulse can be measured. In the subsequent experiments, the pulse energy was varied and the time evolution of plasma parameters was measured.

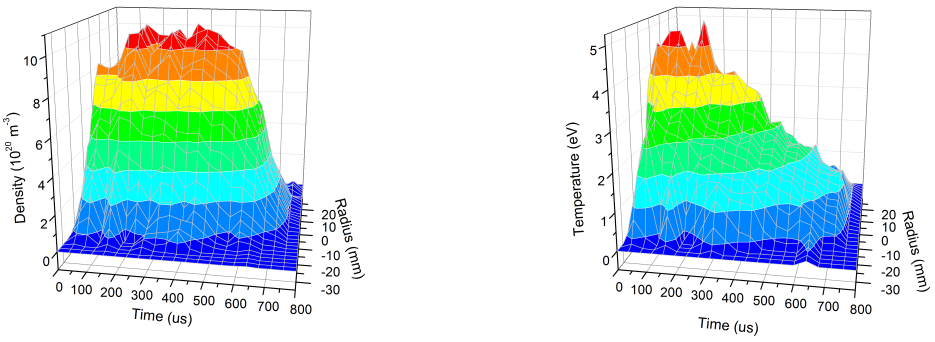

(a) (b)

Figure 3.8: 3D-Plot of the temporal and spatial evolution of (a) electron density and (b) electron temperature during a typical 60 J plasma discharge. The plasma parameters were measured with Thomson scattering, 18 mm in front of the target. The graphs were made by adding measurements of 32 plasma pulses discharged during a single plasma shot. For each plasma pulse, Thomson scattering was performed at a different time interval.

3.2.2 Results

A typical result of a 60 J plasma pulse is shown in figure 3.8a and 3.8b. Here, both electron temperature and electron density rise in approximately 200 μs to peak values of $10.4\pm0.8\times10^{20}$m^3 and 4.6±1.0 eV, respectively, with a FWHM of the beam of 26.3±3.1 mm. The electron density then stays approximately constant until the end of the pulse while the electron temperature decays to the steady-state value. When relating the power dissipated in the source with the plasma pressure near the target, $P_{plasma} \propto n_e T_e$, both seem to behave in approximately the same way, shown in figure 3.9, with peak plasma pressure of approximately 310 Pa.

The energy conversion of dissipated power to increased plasma parameters is investigated by including two energy conversion mechanisms playing a role during a plasma discharge, namely ionization of the gas and heating of the plasma.

First, the gas injected into the plasma source is fully ionized if the power dissipated in the source is sufficient. This can be seen by looking at the evolution of peak electron density during several plasma pulses with different input energies in figure 3.10a and figure 3.10b. For pulses with a pulse energy of 30-120 J, the peak electron density increases rapidly to $\sim10\times10^{20}$m^3, maintaining this value until the end of the pulse. This suggests that the injected gas into the source is fully ionized. For the 15 J pulse, dissipated power is just sufficient to ionize most of the gas because of the lower peak electron density of $\sim10\times10^{20}$m^3. For plasma pulses with higher stored energy, >120 J, the peak electron density is lowered with increasing pulse energy. In this case, one would also expect the gas to be fully ionized because the total energy dissipated in the plasma is still increasing with pulse energy and therefore another phenomenon is observed. A possible explanation for this could be the conservation of the flux of particles. The gas injected into the source is a parameter that is controlled in the experiment and which is fixed throughout a plasma shot. When all gas is ionized, the flux of particles leaving the source is therefore limited by the amount of gas that is injected. It was shown in Pilot-PSI that during a plasma pulse the velocity of ions leaving the plasma pulse is dependent on electron on temperature as $v_{th} \propto T_e^{0.5}$. The ion flux is proportional to $n_e v_{th} \propto n_e T_e^{0.5}$. When the electron temperature is increased, the velocity increases and because the ion flux is limited by the injected gas density decreases.

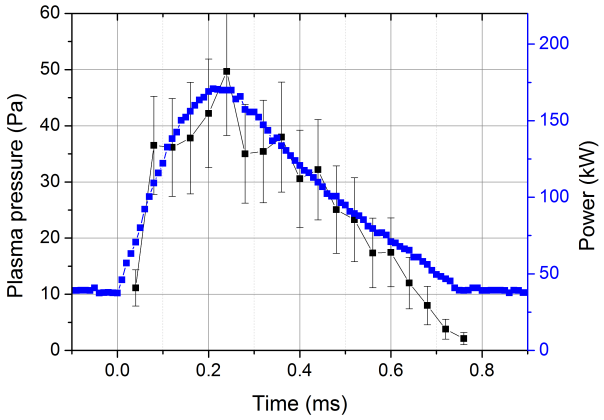

Figure 3.9: A comparison between the peak power dissipated in the plasma and the plasma pressure close to the target. The plasma pressure, $n_e T_e$, was calculated by averaging the peak values measured in the centre of the plasma beam. The plasma pressure, measured 1 m downstream of the source, started increasing simultaneous with the increase of power dissipation. The plasma pressure and dissipated power show to be in good agreement.

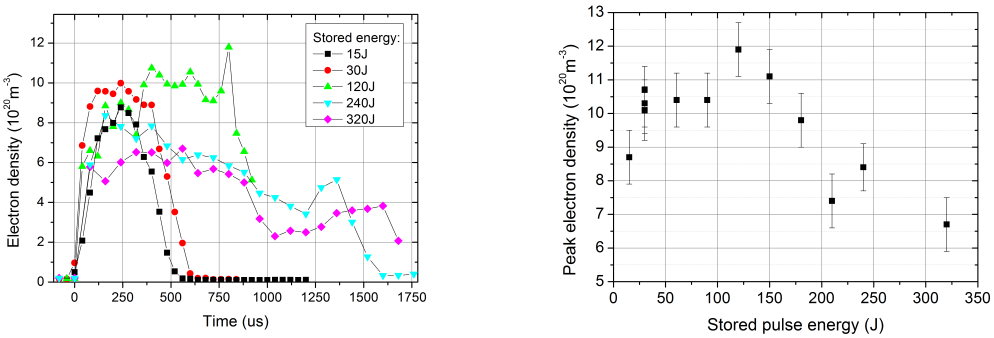

(a) (b)

Figure 3.10: (a) The time evolution of electron density during plasma pulses for several stored energies. Thomson scattering measurements were done 18 mm in front of the target and 10 Standard Liter per Minute (slm) of hydrogen and B-field setting 3 was used in each of the shots. (b) The peak values of the measured electron density evolution for pulses with 15-320 J of energy stored in the capacitors. Pulses with 30-120 J energy reach approximately $n_e = 10 \times 10^{20}$ m^{-3}, whereas the density is lowered with pulse energies >120 J.

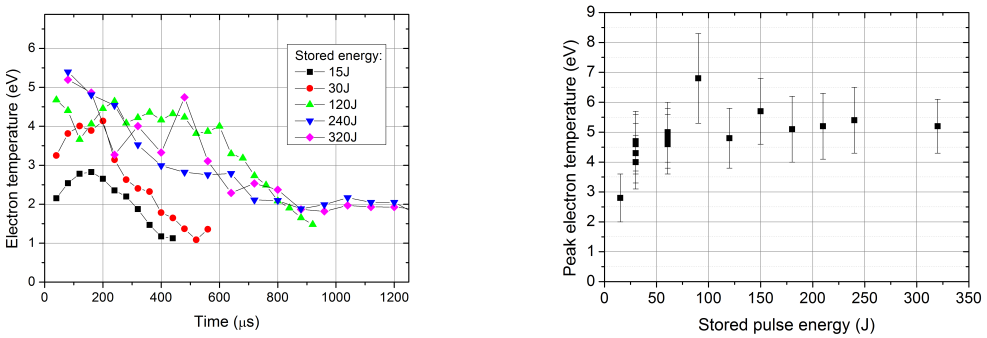

(a) (b)

Figure 3.11: (a) The time evolution of electron temperature for several pulse energies stored in the capacitor, taken from similar shots as in figure 3.10a. Here, the peak electron temperatures are measured early in a pulse and the decay time of the electron temperature increases with pulse energy. (b) The peak values of the measured electron temperature evolution for pulses with 15-320 J of energy stored in the capacitors. Up to pulse energies of 90 J, the peak electron temperature increases. For higher energies, no variation in peak electron temperature is observed.

Similar results are observed in electron temperature and also impact the heat flux as is described in chapter 4.

Second, while in the resonance mode of the pulse the gas is getting fully ionized, the power dissipated in the beam increases the electron temperature of the plasma simultaneous. This is shown in figure 3.11a and figure 3.11b. During the plasma pulses shown in these figures, the highest temperature values are measured at the start of the pulse. The temperatures then decay when the source is in decay mode. For the pulse with 15 J energy the temperature does not increase above ∼3 eV. Because the peak power is in this case just sufficient to fully ionize the gas there is also less stored energy to further heat the plasma. For pulses with energies between 30 to 90 J, the measured peak temperatures rises to ∼7 eV. For larger pulse energies, the temperature does not change significantly with pulse energy. If the gas is fully ionized, the energy needed for full ionization is fixed. Therefore, one would expect the excess power in the source to further increase the electron temperature. This is however not observed in figure 3.11b. It is currently not understood why this is happening. One possible explanation could be due to the lowered electron density along the beam. When the electron density is lowered for higher pulse energy, neutrals will be more likely to penetrate the plasma beam. This could lead to a decrease in electron temperature due to charge exchange and MAR along the beam. The evolution of electron temperature over time also explains the decrease and increase of resistance during a pulse due to the change is Spitzer resistivity, shown in figure 3.6.

To see what the effect of power dissipation on the two energy conversion mechanisms is during the pulse, electron density and electron temperature have been plotted as a function of the power dissipated in the source, shown in figure 3.12a and 3.12b respectively, for several input energies. For the electron density during a 15 and 60 J pulse, a linear increase with input power can be observed during resonance and decay mode when dissipated power <100 kW. For higher power (>100 kW) the density does not increase significantly with additional power. For the pulses with 240 J and 320 J of stored energy, the density is similar to the 15 and 60 J pulses for power <50 kW. For the 240 J pulse and, more pronounced, for the 320 J pulse, a step-like relation

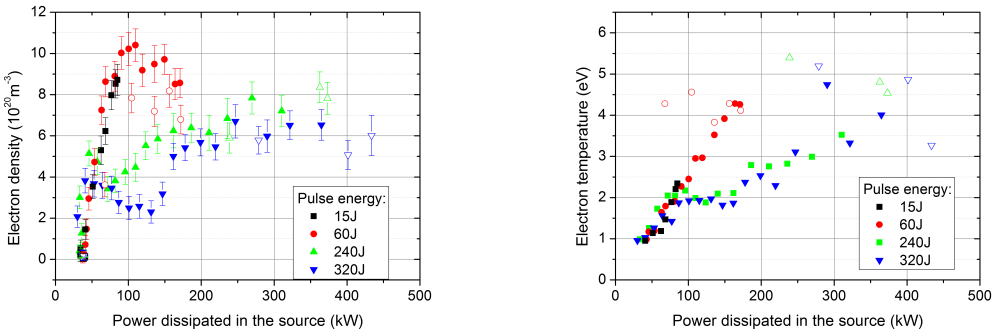

(a) (b)

Figure 3.12: To investigate the effect of dissipated power in the plasma to the change in plasma parameters, the (a) peak electron density and (b) peak electron temperature are plotted here as a function of input power for four different pulse energies. The power dissipated and the plasma parameters measured 18 mm from the target are synchronized. The values measured during resonance mode and during decay mode are distinguished with open symbols and closed symbols, respectively. A different response to the dissipated power can be observed from the 15 and 60 J pulses compared to the 240 and 320 J pulses.

in density around 150 kW can be seen. For higher power (>200 kW) the density also does not increase significantly with dissipated power. For the electron temperature shown in figure 3.12b, both the pulse of 15 and 60 J of stored energy behave the same to input power. The electron temperature increases for increasing input power. Here, the plasma temperature range for the 240 J and 320 J pulse is comparable to the temperatures generated for 15 and 60 J, but similar temperature are generated for much higher power dissipated in the plasma.

The difference in both curves could be explained by the competition between ion velocity and electron density in the beam. For higher pulse energy, the power gradient with time in resonance mode is increasing because peak power is increasing while the rise time remains approximately constant. Because the power gradient is larger for larger stored energies, the plasma is fully ionized more quickly, but also the temperature could increase more rapidly. When the temperature rises more quickly, the peak density will be lower when the plasma is fully ionized because there is a competition between density and ion velocity. When the dissipated power is lower than <150 kW in decay mode, the electron temperature is lowered and the electron density can increase, leading to the step like behaviour and a slight increase in electron density when the power is lowered for the pulse with 320 J of stored energy.

3.2.3 Conclusions and discussion

Thomson scattering measurements near the target were done to measure the evolution of plasma parameters during a plasma pulse. Transiently increased plasma parameters were observed as a result of the transiently dissipated power in the plasma, making the pulsed plasma system a suitable device to replicate ELMs in a linear plasma generator. Peak electron densities were found to range between 6.7-11.9$\times 10^{20}$m-3 and peak electron temperature was found to range between 2.8-6.8 eV. Maximum plasma parameters were generated for pulses with 60-120 J of stored energy in the capacitors.

The results obtained from Thomson scattering in the plasma beam suggest that the gas is

fully ionized and that the remaining stored energy is used to heat the plasma beam. Both electron temperature and electron density are important for the ELM simulations as they both increase the particle and heat flux to the target.

Although it was possible to use single-shot Thomson scattering during these experiments, the error in the measurements is still quite large. Especially when the electron density in the plasma is low, $< 10^{20}$, during the start and end of a pulse, the amount of scattered photons is low and therefore it is hard to get reliable data on electron density and temperature. The electron temperatures for low density were not taken into account and are therefore not shown in the graphs. When looking at the time evolution of the peak plasma values, it should also be noted that each data point was obtained from a different plasma pulse. It is assumed that for each pulse the evolution is reproducible. This assumption will also lead to an additional error in time and in peak values obtained.

In both the graphs showing time evolution and the relation between plasma parameters and power dissipation it should be noted that the start of the pulse (t = 0) was empirically determined as the last data point where the electron density had a steady-state electron density ($\sim 0.2 \times 10^{20} m^3$). The time required for the particles to travel from the source to the line of sight of the Thomson laser is about 50 μs, assuming that the axial velocity is 20 km/s which was measured from the pulsed plasma in Pilot-PSI, although an instantaneous increase of parameters was observed in figure 3.9. It was also shown that the velocity scales with electron temperature as $v_{th} \propto T_e^{0.5}$ [24] which could explain the lower electron density for higher pulse energy.

The current results show that temperatures of 6.8 eV and densities of up to 1.2×10^{21} m^{-3} can be reached with B-field setting 3 and hydrogen gas flow of 10 slm. This is, however, still much lower than the values obtained in Pilot, where peak parameters of 12 eV and 5×10^{21} m^{-3} have been measured near the target using the same gas flow and a 33% higher B-field. The main reason for the lower peak parameters measured in Magnum-PSI is likely the expanding B-field that is currently present near the position of the target due to the current magnet configuration. At the position of the Thomson laser, the axial magnetic field strength is 5-7 times lower than the magnetic field strength in the linear field. Assuming that most of the plasma is confined to the B-field and using $\nabla \cdot B = 0$, it can be found that

$$n_{e,centre} = n_{e,target} \frac{B_{centre}}{B_{target}}, \tag{3.4}$$

where *centre* denotes the parameters within the centre of the magnets, in the linear magnetic field, and *target* denotes the parameters at the location of the target, in the diverging magnetic field. This means the electron density in the linear magnetic field should be 5-7 larger than the electron density at the location where Thomson scattering measurements are performed. The peak electron density during a plasma pulse is a factor 6 higher near the target in Pilot-PSI, but in Pilot the B-field is linear. This suggests that these values are in line with the expected electron density of Magnum-PSI in the linear magnetic field. The expanding plasma will furthermore cool down fast, which can explain the lower electron temperature near the target observed in Magnum-PSI compared to the electron temperature near the target in Pilot-PSI. The effect of the expanding B-field is discussed more extensively in section 4.2.1.

3.3 The effect of the target

3.3.1 Experimental methods

As was shown in Pilot-PSI [24], the presence of a target in the plasma greatly influences the plasma parameters during a plasma pulse. In this section, the effect of the target on the plasma

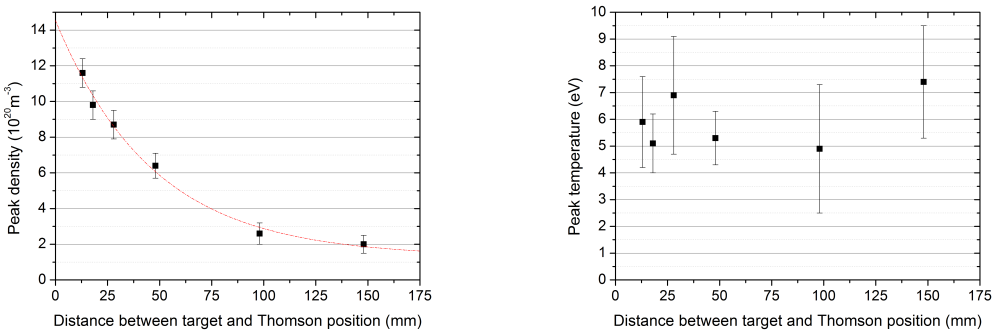

(a) (b)

Figure 3.13: By increasing the distance between the target and the fixed position of Thomson scattering, the effect of the target on the plasma parameters is investigated. (a) Peak electron density and (b) electron temperature values for a 180 J plasma pulse are shown here while the target is retracted from 13 to 148 mm from the Thomson position. The temperature was not found to vary much due to the presence of the target, while the electron density decreases exponentially as $n_e \propto e^{x/0.047}$.

parameters close to the target is investigated. Knowing the plasma parameters and understanding what processes are going on in the plasma close to the target will lead to a better understanding of the temperature response and the surface modifications of the target due to the increased heat and particle flux during a plasma pulse.

In Magnum-PSI it is possible to control the position of the target with respect to the axis along the plasma beam. By increasing and decreasing the distance between the target and the Thomson scattering measurements, the effect of the target on the plasma can be isolated from the other processes occurring in the beam. Here, the target is retracted while all input parameters remain constant. Thomson scattering is performed on a fixed axial position in the beam, ∼1 m downstream from the plasma source. A fast visible camera with H_α is monitoring the target perpendicular to the axis of the plasma beam to investigate the effect of reflected neutrals from the target.

3.3.2 Results

Figure 3.13a shows the maximum values found for electron density during a pulse as a function of distance. The peak electron density decreases with increasing distance from 12×10^{20} m^{-3} at 13 mm to 2×10^{20} m^{-3} at 148 mm, indicating that the presence of the target is clearly influencing the electron density profile, increasing the electron density with at least a factor six near the target. The average FWHM of the beam decreases from 24.1 mm to 20.9 mm for these distances. As shown in figure 3.13b, the peak electron temperature is not influenced by the target distance, however. Here the electron temperature does not change significantly, with peak values of approximately 6 eV.

One can assume that the total flux of particles at the position of Thomson scattering scales as $\Gamma_{ion} \propto n_e v_{th} R_{beam}^2$ in the plasma beam. When the input parameters of the pulsed plasma system are not changed, Γ_{ion} is not expected to change. When the target is present, however, the total flux is increased due to the electron density increasing with a factor 6 while the electron temperature and FWHM of the beam do not change significantly. This means there is an

additional source of particles due to the presence of the target.

The source of the increase of electron density can possibly be attributed to the ions and electrons being reflected at the target. Two mechanisms at the target are considered here: Sputtering of atoms and reflection of neutralized ions coming from the plasma beam. At peak temperatures of around 6 eV and with the target at floating potential, sputtering of tungsten atoms is not possible with hydrogen ions. The particle reflection coefficient, however, is higher than 76% for these energies [34], which would yield a total fluence of $\sim 2 \times 10^{25} \mathrm{m}^{-2}\mathrm{s}^{-1}$ of neutral hydrogen atoms and molecules in the centre of the beam. The reflected particles are ionized again, increasing the plasma density. This would likely make it a significant source of ions.

The effect of the target as a source of particles is more closely investigated in figure 3.14. The electron density is higher when the distance is lower throughout the total duration of the pulse. For the pulse traces with the target at 13 and 48 mm distance, the peak density remains constant until $\sim$200 μs. After the power dissipated in the source is maximum, the peak electron density is transiently increased after $\sim$200 μs. This effect is however not observed when the distance is very large, as shown for the density evolution at 148 mm distance.

We would like to know why the electron density is transiently increased after 200 μs. Because the time-of-flight for reflected particles between Thomson scattering position and target is in the order of a few microseconds, this will likely influence the electron density instantaneously. A possible explanation for this phenomenon could be that for these pulse energies the electron temperature quickly decreases when power is decreasing. The drop in electron temperature would then decrease the ion velocity and therefore increase the electron density due to conservation of incoming particles from the plasma beam when the gas is fully ionized.

The distance from the target for which the influence of increased electron density can be observed is at approximately <100 mm in front of the target. This value is larger then expected from theory and experiment. When hydrogen ions arrive at the target, most ions will be neutralized into a H^0 atoms or recombine to a H_2 molecule. During this process, an H_α photon with a wavelength of 656 nm will be emitted. In figure 3.15 it is shown that most of the recycling of neutrals and charge exchange take place at approximately 200 μm in front of the target, and it seems that for a distance >4 mm in front of the target all neutrals are ionized. In literature it is also found that $\lambda_{ionization} \approx 4.4$ mm for hydrogen in these high densities [35], using an energy reflection coefficient of 0.8 and the plasma parameters as measured with Thomson scattering. Therefore one can conclude that all neutrals from the target are re-ionized before arriving at the measurement position. The re-ionization event cools down the plasma, but as this is happening for distances < 13 mm a change of electron temperature is not observed. The re-ionized particles could, however, contribute to the electron density if some of the ions maintain a velocity component away from the target after re-ionization at a distance of $\sim$100 mm.

With the retractable target it is also possible to investigate the current path of the electron beam. One would expect that, due to limited radial transportation in the plasma beam when the magnetic field is switched on, most of the current is driven in the plasma beam to the target. This is, however, not observed in Magnum-PSI as shown in figure 3.16. Here the peak resistance remains between 0.16-0.17 Ohm while the current path is increased by retracting the target.

Because the total resistance is proportional to the length of the current path, equation (3.3), the total resistance is expected to increase when the target is retracted. The radial transportation of electrons is described by the Hall parameter, H_e. When the Hall parameter is high enough, radial transport of electrons in the plasma beam is limited until the current is 'shorted' by the conducting target [33]. The Hall parameter is defined as the ratio between the electron cyclotron frequency and the collision frequency, which for electrons is [31]

$$H_e = 9 \times 10^{21} \frac{B(kT_e)^{3/2}}{n_e}. \tag{3.5}$$

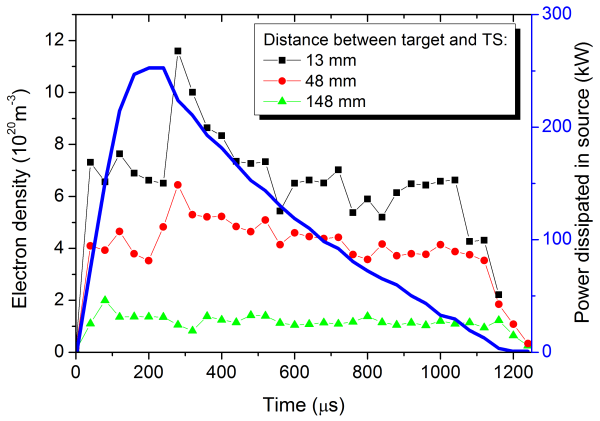

Figure 3.14: To investigate the electron density in greater detail, the time evolution of the electron density for a distance of 13, 48 and 148 mm is shown here. The density is lowered with increasing distance throughout the pulse. After 200 μs, an increased electron density is seen for distances <50 mm. The power dissipation in the beam is shown by the solid line as an indication of the pulse duration.

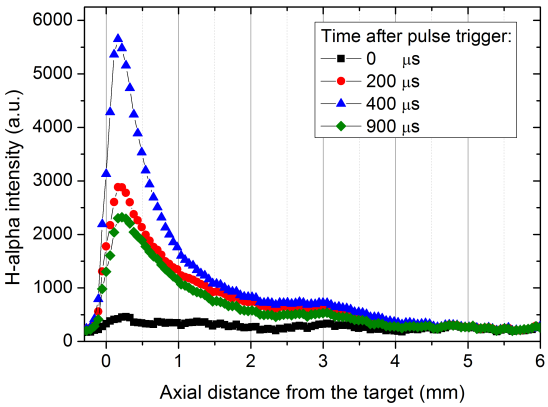

Figure 3.15: H_α emission measured with a fast-camera as a function of axial distance from the target to show the depth of re-ionization in the plasma. The direction of sight of the camera was perpendicular to the axis of the plasma beam. Several curves with respect to time after the trigger of the 108 J pulse are shown here. The graph shows that almost all of the reflected neutrals are re-ionized approximately 3 mm in front of the target.

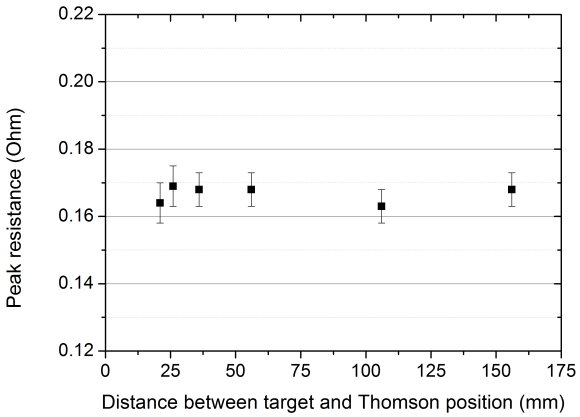

Figure 3.16: Plot of plasma resistance during the retraction scan to get an indication of the amount of electrons 'shorted' through the target. The resistance of the plasma is measured between cathode and anode as a function of distance between the fixed Thomson measurement position and the retracted target for plasma pulses with 180 J of stored capacitor energy. Because the resistance stays approximately constant, it is likely that a very small amount of current flows through the target.

Due to the diverging magnetic field near the target, the Hall parameter at the Thomson scattering position, which is approximately 26 close to the target, is probably too low to limit radial transportation of electrons before the plasma reaches the target. In Pilot-PSI, where most of the electron current is assumed to flow through the target, a Hall parameter of 83-125 was found [24]. A higher B-field is needed to have more electron current passing through the target.

3.3.3 Conclusions and discussion

The results from the retraction scan show that the electron density is greatly influenced by the presence of a target in the plasma beam. Although the electron density was found to increase from approximately 2×10^{20} m^{-3} in the beam to at least 12×10^{20} m^{-3} close to the target, the peak electron temperature at 6 eV was not significantly affected by the target at the distances investigated in this thesis. It was furthermore shown that little electron current passes through the target during a plasma pulse.

The increase in density could be explained by reflected particles which are re-ionized, but figure 3.15 shows that almost all neutrals are re-ionized 3 mm in front of the target. Although the velocity of the re-ionized particles will be directed along the electric field, it one explanation could be that some ions maintain a velocity component towards the source at a distance of 10 mm away from the target. Although it would be interesting to measure the plasma parameters closer to the target, it is difficult to further decrease the distance between the target and the Thomson measurement due to the increased amount of scattered light from the target.

The effect of reflected particles has also been observed in Pilot-PSI and could limit the heat/particle flux towards the target due to cooling of the plasma near the sheath entrance. Although the temperature does not seem to be affected 13 mm away from the target, it might be possible that this is the case near the sheath entrance, which is in the order of a few μm from the target. Unfortunately, the Thomson system is not able to measure at these distances. Another

effect that limits measurements when the target is retracted to a distance of > 100 mm is the low electron density. Because low electron density implies less scattered light from the ions, the relative error of both density and temperature becomes increasingly large. The results at these distances are therefore less reliable.

Chapter 4

Target response to the pulsed plasma

4.1 Experimental methods

In the previous chapter it was shown that the pulse plasma system in Magnum-PSI allows for the generation of transiently increased electron densities and temperatures, making it a suitable setup to simulate ELMs. It was furthermore shown that the presence of a target in the plasma affects the electron density significantly. In this chapter, the response of the target surface to these changing plasma parameters will be investigated in more detail.

The goal of this chapter is to understand the response of the target to the changing plasma parameters during a plasma pulse in Magnum-PSI. First, the heat flux to the target will be investigated by changing the pulse energy stored in the capacitor bank. This should lead to a better understanding of the range of heat and energy fluxes that can be generated with the pulsed plasma system and should allow us to find the optimal settings to generate ITER-like pulses. Second, the time evolution of plasma parameters that were measured with Thomson scattering are related to the temperature evolution of the target. This will allow us to find the sheath heat transmission coefficient and will validate the electron density and electron temperature evolution found in the previous chapter. In the previous chapter it was furthermore found that the B-field does play a role in the evolution of plasma parameters near the target. The effect of the magnetic field that is currently present in Magnum-PSI to the heat fluxes that can be obtained is investigated. This was done to extrapolate the results found for the copper magnets to the results expected when the superconducting magnet is installed.

In these experiments, polished tungsten disks were used with a thickness of 1 mm and a diameter of ⌀30 mm. The response of the target surface to pulsed plasmas was mainly investigated by measuring the temperature evolution of the target. This was done with the fast IR-Camera measuring with 7468 Hz. Knowing the temperature evolution, the net heat flux to the target can be calculated through the THEODOR numerical code for specific materials.

4.2 Results

Figure 4.1a shows the temperature evolution of a tungsten target during a plasma shot in Magnum-PSI. The magnetic field is switched on for approximately 6 seconds leading to a steady-state temperature, T_{base} of ∼280 °C. After 1.07 seconds, the capacitor bank is triggered and starts to superimpose plasma pulses on the steady-state plasma with a repetition rate of 8 Hz. The average temperature increase, ΔT_{pulse}, found during this shot was 173±8°C. A single pulse

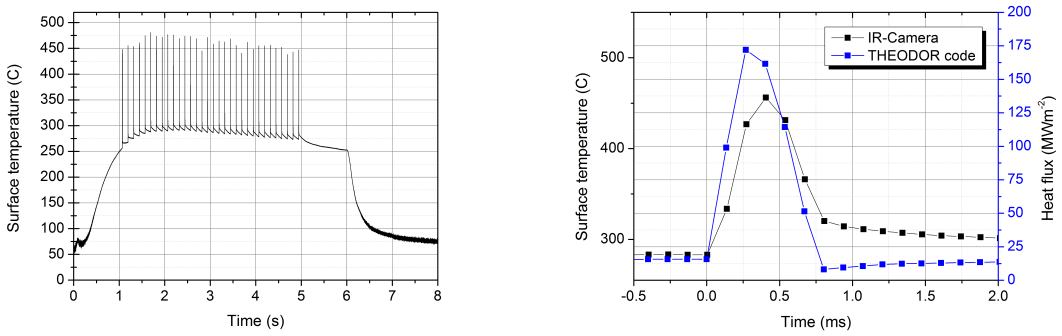

(a) (b)

Figure 4.1: (a) Typical temperature evolution of a tungsten target surface during a full plasma shot. Here, B-field setting 2 was used with 200 A of steady state current and 60 J pulses were discharged. (b) A close-up of the 20^{th} pulse in the shot of picture (a). In the same graph the calculated heat flux by the THEODOR code is shown.

during this shot is shown in more detail in figure 4.1b. The temperature increases in ∼400 μs to a peak value of 456°C and then decays exponentially to T_{base}. In this figure, the peak heat flux as calculated by THEODOR is also shown. Here the heat flux from the plasma is 16 MWm^{-2} in steady-state and increases to 172 MWm^{-2} during the plasma pulse. Because THEODOR takes heat conduction from the surface to the bulk of the target into account, the heat flux pulse to the target has returned to its steady-state value after ∼800 μs while the target is still cooling down to T_{base}.

The peak heat flux during a pulse is one of the parameters that should be matched to the values as expected in ITER (1-10 GWm^{-2} during type-I ELMs [11]) to simulate ITER-like ELMs. For plasma operation in B-field setting 3, however, the highest averaged peak heat flux found was 180±7 MWm^{-2}, as shown in figure 4.2. Here, the maximum heat flux was found for pulses with 30 to 60 J of stored energy, while for pulses with higher energy the peak heat flux was found to decrease slightly to 142 MWm^{-2} for a 240 J pulse. This effect is similar to the peak plasma parameters found in section 3.2.2 from Thomson scattering measurements near the target. Although peak electron temperature stays approximately constant for pulse energies above 60 J, the peak electron density decreases for pulse energies $>$ 120 J, decreasing the heat flux to the target.

When integrating the calculated heat flux evolution over time, the peak energy density to the target during a pulse is found. The peak energy density for different pulse energies is shown in figure 4.3. The energy density increases with pulse energy to about 62±5 kJm^{-2} for a 120 J pulse after which the energy density remains approximately constant with increasing pulse energy. Two factors play a role in the energy flux to target: the pulse duration and the peak heat flux. The pulse duration increases for decreasing resistance, which is the result of the increased electron temperature in the plasma beam. Because the peak heat flux decreases for pulse energies $>$ 120 J, as shown in figure 4.2, one can expect that the energy flux will not increase of decrease significantly for increasing pulse energy.

To see what the effect of the plasma parameters is on the target, the evolution of the heat flux from the IR-Camera is compared with the evolution of plasma parameters. The data obtained from Thomson scattering and the heat flux evolution at the target surface can be compared

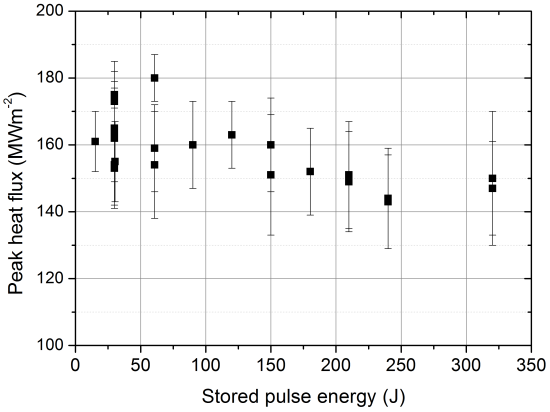

Figure 4.2: The peak heat flux at the target due to plasma pulses versus stored energy in the capacitors. The peak heat flux is the maximum heat flux calculated with THEODOR from the images recorded with the IR-Camera. During all of shots shown in this graph, B-field setting 3 was used and a single capacitor was discharged for each pulse. The peak heat flux decreases slightly with increasing energy and peaks at 180 MWm^{-2} for 60 J pulses.

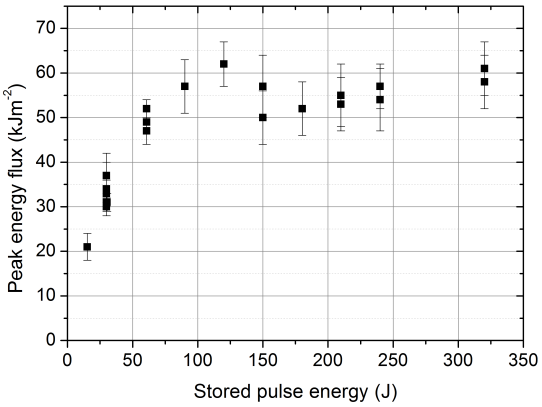

Figure 4.3: To include the effect of the variable pulse duration, peak energy flux was plotted as a function of stored pulse energy. The energy flux was calculated by integrating the heat flux evolution to the target with time for the entire pulse duration. A peak energy flux of approximately 62 kJm^{-2} for 120 J pulses is measured. For higher pulse energy there is little variation.

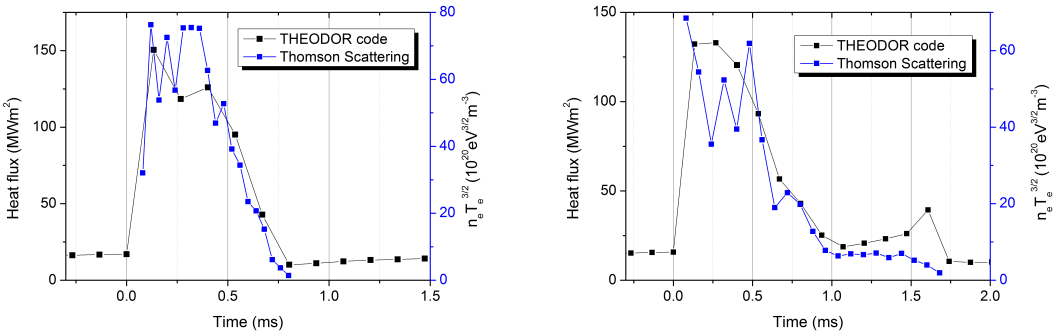

Figure 4.4: To calculate the sheath heat transmission coefficient, the heat flux evolution of a (a) 60 J pulse and (b) 320 J pulse was compared to the heat flux parameters, $n_e T_e^{3/2}$, as measured with Thomson scattering, 18 mm in front of the target. Both seem to be in good agreement with $q \approx 2.2 \times 10^6 n_e[10^{20} m^{-3}] T_e^{3/2}[eV^{3/2}]$

according to

$$q = \gamma k T_e \Gamma_{se} \approx (\frac{2}{3m_i})^{1/2} \gamma n_e (kT_e)^{3/2}, \tag{4.1}$$

where q is the heat flux to the surface, γ is the sheath heat transmission coefficient, Γ_{se} is the particle flux to the surface, and m_i is the ion mass [35]. Here, an adiabatic plasma is assumed with $T_e \approx T_i$. The latter assumption is valid because of the high collisionality between electrons and ions during pulse due to the high electron density [36].

The sheath heat transmission coefficient can be determined by comparing the heat flux measured with the IR-camera to the heat flux one would expect from the plasma parameters as measured with Thomson scattering. This has been done for the evolution of a 60 J pulse and a 320 J pulse, plotted in figure 4.4a and figure 4.4b, respectively. Both heat flux evolutions calculated with THEODOR seem to behave quite similar to the heat flux obtained from Thomson scattering, where $q \approx 2.2 \times 10^6 n_e[10^{20} m^{-3}] T_e^{3/2}[eV^{3/2}]$. Taking into account the correct dimensions and the mass of hydrogen ions, the sheath heat transmission coefficient was determined as $\gamma \approx 17$. This value is larger than the sheath heat transmission coefficient found in Pilot-PSI, which is ranging between 3 and 12 for hydrogen in steady-state operation [37]. This would imply that the electron density near the sheath entrance is higher than the electron density at the Thomson position, which is confirmed in section 3.3. Figure 4.4b furthermore confirms that the effect of the lowered density as observed from Thomson scattering in the beam is observed at the target. The increased pulse duration due to the increased decay time for higher pulse energies measured from the I-V characteristics are also measured with the IR-Camera at the target.

To assess whether an increase in pulse duration for increasing pulse energy is also observed in the temperature evolution above the surface temperature in steady-state, the duration of the temperature increase at the target was investigated and related to the pulse duration from the I-V characteristics at the source, as shown in figure 4.5. Here the total pulse duration measured from the power dissipated and the IR-Camera is defined as $\tau_{Source/IR} = \tau_{ramp} + \tau_{decay}$ which is derived from the current trace during a pulse and the increased temperature above the base temperature from the IR-Camera. A linear increase between τ_{Source} and τ_{IR} is observed for $\tau_{Source} < 710$ μs. The rate with which τ_{IR} increases is however much larger. For a pulse of 450 μs in the source,

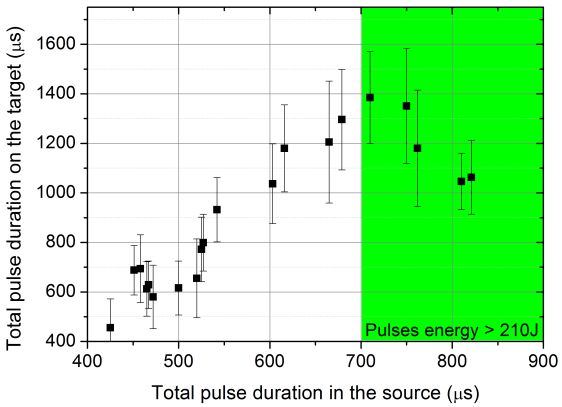

Figure 4.5: Graph to assess the increase in pulse duration between the power dissipation, as measured from the I-V characteristics in the source, and the temperature increase at the target as measured with the IR-Camera at the target surface. The total pulse duration is defined as the combined ramp-up and decay time. A linear increase is observed for pulses where the pulse duration in the source is 710 μs, while a decrease is observed for larger pulse duration in the source. The green region depicts the values for which pulse energies were larger than 210 J.

the duration of the temperature increase is also 450 μs. For a pulse duration of 720 μs in the source, however, the pulse duration at the target is approximately 1400 μs. It is currently not understood why this is happening. A similar increase in pulse duration has been found for ELM simulation experiments with pulsed lasers and simultaneous steady-state plasma. The reason for this effect is currently investigated.

For pulse energies >210 J, the drop in electron density in the beam when the pulse is in decay mode causes the heat flux to the target to be strongly reduced, as can be seen from the rapidly decaying heat flux in figure 4.4b and the step-like decrease of resistance for decreasing dissipated power around 150 kWm^{-2} as shown in figure 3.12a. This results in a drop of flux to the target while the decrease in resistance along the plasma beam for higher pulse energy does increase the decay time of the power dissipated in the beam.

4.2.1 The effect of B-field on the heat flux to the target

Currently, it is expected that one of the main limitations of the peak heat flux to the target in Magnum-PSI is the diverging B-field near the target position. To validate this, the effect of an higher B-field on the peak heat flux to the target is investigated. This will furthermore give an indication whether the superconducting magnet will allow the pulsed plasma to reach the heat/energy fluxes that are expected during type-I ELMs in ITER. The effect of the diverging B-field that is currently present at the position of the target, can be investigated in two ways. First, the B-field can be increased by increasing the current in the copper coils. This will not decrease the divergence of the magnetic field lines. As was shown in section 3.3, an insignificant share of the electron current passes through the target. This is most likely due to the low Hall parameter near the target. Increasing the Hall parameter by increasing the magnetic field strength will limit radial transportation and thereby increase the electron current through the target. It does, however, limit the duration of a shot as the copper coils heat up faster due

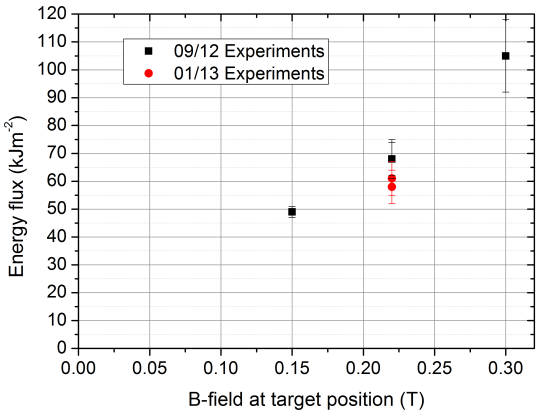

Figure 4.6: Assessment of the effect of a stronger B-field on the energy flux to the target. The peak energy flux to the target surface is plotted for increasing B-field strength by an increased current through the magnetic coils. The target has a distance of 18 mm from the Thomson scattering position and the stored pulse energy is 324 J. An increase in energy flux is observed for increasing B-field strength.

to Ohmic heating. Second, the axial magnetic field at the target surface can be increased by inserting the target further towards the copper coils and into the linear magnetic field. This does also decrease the divergence of the magnetic field, removing the radial velocity component of the confined particles and increasing the electron density due to the decreased diameter of the plasma beam, but disables the use of Thomson scattering.

In figure 4.6 the peak energy flux is shown for different B-field settings while the target is at constant position. Here, the flux to the target is more than doubled when the B-field is increased at the target position from 0.15 T to 0.30 T. There appears to be a linear increase of energy flux to the target with B-field strength that goes to 0 kJm−2 when no B-field is present. The reason for the linear increase between B-field strength is probably due to the increased Hall parameter. As the Hall parameter, which limits radial transport of particles, perpendicular to the magnetic field lines, is directly proportional to the strength of the B-field, equation (3.5), more particles will arrive at the target with higher B-field. This will increase the electron density close to the target and hence the heat/particle flux to the target.

In figure 4.7 the peak energy flux at the target is plotted for several positions of the retracted target. In this case, a 16% increase of the axial B-field strength at the target position causes the energy flux to increase with approximately a factor 2.5. The increase in energy flux is much larger than would be expected from equation (3.4). One possible explanation for this increase is that in the low field region, where the plasma is expanding, the effect of MAR and charge exchange is increased. This will cool down the plasma, leading to less energy flux going to the target. Another explanation for this observation is the increased radial B-field, giving the ions confined to the B-field a radial velocity component. The neutralized particles will be reflected perpendicular to the target due to the perpendicular acceleration in the sheath. The reflected particles will then further increase the width of the beam and will not contribute to the peak electron density in the centre of the beam. This could lead to an additional decrease of peak energy flux to the target when the target is retracted.

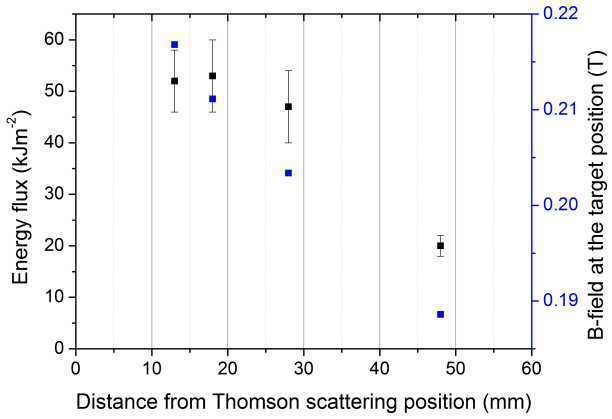

Figure 4.7: The peak energy flux to the target when the target is retracted to investigate the effect of the diverging B-field at the target position. The distance of the target from the Thomson scattering position is stated on the x-axis, while the corresponding axial B-field strength at the target position is stated on the right y-axis. B-setting 3 was used and the stored pulse energy was 180 J. The energy flux increases with a factor 2.5 when the distance is decreased from 48 mm to 13 mm.

4.3 Conclusions and discussion

The results obtained with the IR-Camera show that the setup of Magnum-PSI is able to simulate periodic ELMs with a simultaneous steady-state heat/particle load. The requirements for ITER, however, are not yet met and seem limited by the magnetic field at the target. With the target 18 mm in front of the Thomson laser, using B-field setting 3[1] and 10 slm of gas flow, it was not possible to obtain higher heat fluxes than 238±46 MWm^{-2}, and energy fluxes of 68±7 kJm^{-2} for a 1 ms pulse without damaging the nozzle of the plasma source. This while the heat and energy flux during a type I ELM in ITER are expected to be 1-10 GWm^{-2} and 10 MJm^{-2} for 1 ms [30], respectively. The typical energy densities, in the order of 100 kJm^2 [38], due to type-I ELMs as observed in JET, however, are reached when the target is inserted further into the linear magnetic field. That inserting the target further into the linear magnetic field does increase the heat flux will be shown with the experiments on ITER-monoblocks in chapter 5. This gives reasonable confidence that the pulsed plasma system will reach the conditions expected for ITER when the superconducting magnet is installed.

There is empirical evidence from Pilot-PSI confirming that the heat and energy fluxes of such a system can reach ITER-like conditions. In Pilot-PSI the magnetic field at the target can reach values of 1.6 T, compared to 0.3 T in Magnum-PSI. Although there are more neutrals in the vacuum vessel of Pilot-PSI, it is possible to obtain peak heat and energy fluxes of up to 1.5 GWm^{-2} and 771 kJm^{-2} for 1.5 ms, respectively [24]. In Pilot, a drop of energy flux with increasing pulse energy is also observed which is attributed to self-shielding due to the desorption of trapped hydrogen atoms. The electron densities and heat fluxes in Magnum-PSI are currently too low, however, to observe such effects.

Peak electron temperature during a scan of pulse energy in Pilot-PSI is shown in figure 4.8a.

[1] B-field setting 3 is maximum setting that is currently allowed on Magnum-PSI for fear of damaging the magnets.

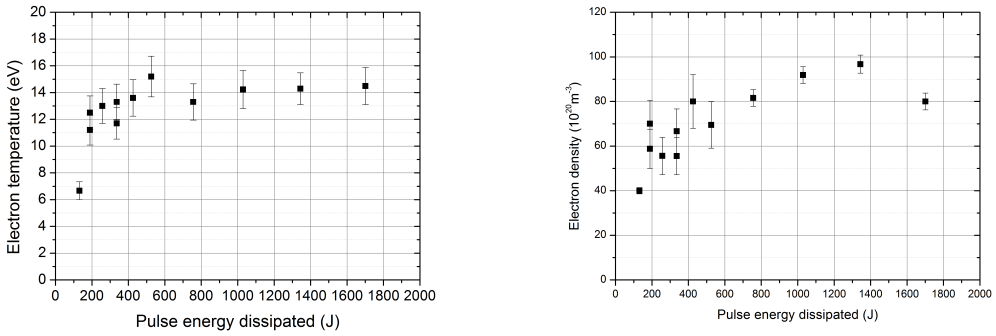

(a) (b)

Figure 4.8: The peak (a) electron temperature and (b) electron density as a function of dissipated energy in the source measured from pulsed plasmas in Pilot-PSI as a comparison with the plasma parameters obtained in Magnum-PSI. The measurements were done with Thomson scattering 4 cm in front of the source with 1.6 T B-field strength. The electron temperature behaves similar to dissipated pulse energy, although the temperature observed is much higher. The electron density, however, does not decrease with pulse energy which contradicts the observations found for peak electron density in Magnum-PSI.

Here the electron temperature is also shown to stop increasing with pulse energy for >200 J per pulse. The temperatures around 14 eV are much higher compared to the temperature measured in Magnum-PSI which is approximately 5 eV. If one assumes that the response of plasma parameters close to the source is similar in Magnum and Pilot and the plasma temperature close to the source would also be 14 eV in Magnum-PSI, this would suggest that there is significant cooling along the beam in Magnum-PSI.

The electron density in Pilot-PSI is shown in figure 4.8b. The electron density, however, does not decrease with energy as was observed in figure 3.10b and which is attributed to the limited particle flux for a fully ionized gas. Why this is not happening, while here also particle flux for a fully ionized gas is limited, is currently not understood.

To see how the pulsed plasma response of the target compares with other ELM simulation experiments, the temperature increase as a function of energy flux for pulsed plasma and pulsed laser experiment is compared in figure 4.9. In both experiments, a tungsten disk was used as a target. During the pulsed laser simulations, a Nd:YAG laser with controllable pulse energy and 1.5 ms pulse duration was fired at the target under an angle with the normal of the target surface while it was exposed to a simultaneous steady-state plasma. The expected peak energy flux to the target during a pulse from the laser can be calculated from the pulse energy of the laser. During the pulsed plasma simulations, the heat flux was calculated from equation (4.1) using $\gamma \approx 17$. When integrating the peak heat flux over time, one can find the peak energy flux during the pulse. The temperature increase was in both cases measured with the fast IR-Camera.

Two things can be observed from figure 4.9. First, the peak energy flux to the target can be much higher for pulsed lasers as compared to the pulsed plasma. The peak power flux of the laser can be as large as a few GWm^{-2} and over time the flux evolution is a *top-hat*, meaning that for 1.5 ms the peak power flux remains constant and then drops to zero. For the pulsed plasmas the pulse duration is varying between 400 ms and 1000 ms while the power evolution over time is peaked. This makes the two systems difficult to compare. The range and flexibility

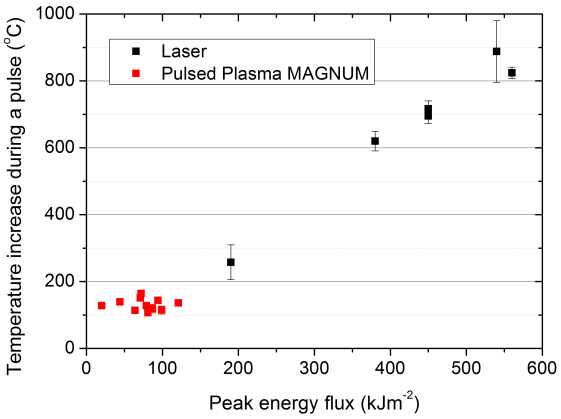

Figure 4.9: A comparison of pulsed laser and pulsed plasma ELM simulations in Magnum-PSI, shown by the temperature increase at the target surface as measured with IR-Camera as a function of peak energy flux to the target. The energy flux for the pulsed plasmas is calculated from the Thomson measurement data and the sheath heat transmission coefficient, while the energy flux from the pulsed laser can be calculated when knowing the pulse energy and the pulse duration. The pulse duration of a laser pulse is approximately 1.5 ms while the duration of the pulsed plasma ranges between 400 and 900 ms.

of pulsed lasers in terms of heat and energy flux is one of the main reasons why lasers are often used for ELM simulations.

Second, the temperature response to the incoming pulse between the two simulations methods is very different. Whereas the temperature increase with energy flux for laser pulses is approximately linear, this is not observed for the plasma pulses. The later effect is mainly due to the increasing decay time of a plasma pulse with increasing pulse energy while the peak heat flux is not increasing. The longer decaying tail of power flux to the target will probably not increase the temperature of the surface. If the temperature increase of the surface is assumed to be linear with energy flux of the laser pulse, the plot does show that the calculated sheath heat transmission coefficient is approximately correct. This implies that the heat fluxes calculated with THEODOR are also correct.

The results obtained from THEODOR come with an error bar which is mainly due to the empirical determination of α_{top}. For most of the measurements shown in this chapter (B-field setting 3, the target at 18 mm distance from the Thomson position, and 10 slm of hydrogen gas flow), the parameter was determined as $\alpha_{top} = (1.5 \pm 0.2)$ $\mathrm{MWm^{-2}K^{-1}}$ using the method explained in section 2.3.2. The actual parameter and the subsequent calculated heat fluxes could therefore differ from the values stated here when a different α_{top} is chosen. The observed behaviour of the peak heat fluxes as a function of pulse energy, nonetheless, is the same regardless of the value of α_{top}. Moreover, the energy flux does not depend on α_{top}.

In some of the measurements, it is hard attribute the effects of heat flux due to a plasma pulse to the target surface solely to the physics in the plasma. In many of the experimental campaigns, the nozzle broke down, or impurities were observed for too high pulse energies or when operating with too high gas flows. Therefore, some of the measurements done were not shown in this thesis, because it was not clear at what point during the measurement the source broke down. During some experiments, impurity lines of copper around 532 nm were observed with the ICCD

camera from Thomson scattering during peak power being dissipated in the plasma during a plasma pulse. A lot of effort has been put into the optimization of the nozzle material. At this moment, a tungsten coated (200 nm) nozzle of Cu/W seems the most promising candidate, producing little impurities and having the longest life-time in pulsed operation if non-destructive input parameters are used. With this source design, it was possible to do experiments on the ITER monoblocks with magnetic field for almost 40 minutes and 17600 pulses without any signs of damage or impurities.

Chapter 5

Applications of the pulsed plasma systems

In the previous chapters the characteristics of pulsed plasmas were discussed and the effect of these pulsed plasmas to the temperature evolution of the target was analysed. ITER-like conditions were not yet reached in Magnum-PSI, mainly due to the constraint of the diverging B-field near the target that is currently confining the plasma beam, but the transiently increased particle/heat source with simultaneous steady-state plasma is shown to be a suitable device to replicate ELM-like conditions expected in a divertor. As the response of the target to the pulsed plasma is known, several experiments on targets were done to answer key questions of concern in the ITER divertor, which will be presented in this chapter.

In section 5.1, 'fuzz' samples, which have been created by helium exposure in NAGDIS-II, were tested in Magnum to study the thermal behaviour of nano-structures on tungsten surfaces exposed to pulsed plasmas. These experiments were done in collaboration with Shin Kajita from the Nagoya University in Japan. A success for Magnum-PSI and the pulsed plasma system was the exposure of ITER monoblocks to >17000 plasma pulses to assess the performance after a large amount of transient events. The preliminary results from the first set of experiments will be presented in section 5.2. This was done to test the effect of recrystallization events with transient pulsing of the ITER monoblocks. Finally, the effect of transient melting of tungsten targets is investigated in section 5.3. The experiments were done on the pulsed plasma system in Pilot-PSI to access ITER-like heat loads expected for type-I ELMs. The goal of this experiment was to analyse the mobility of the melted layer during a transient event and to quantify the amount of melted material due to such an event as a function of the number of transient melting events.

5.1 'Fuzz' samples in Magnum

To investigate the damage due to pulsed plasmas, 'fuzz' samples were exposed in Magnum-PSI. The experiment was done in collaboration with the Nagoya University in Japan. In this experiment, three targets were prepared with NAGDIS-II, a linear plasma device at the Nagoya university. The tungsten targets had a diameter of ⌀30 mm with a thickness of 0.2 mm. Sample 1, was polished and not exposed to any plasma. Sample 2 and 3 were exposed to a fluence of helium ions of $10^{26}\mathrm{m}^{-2}$ at $T_{surface} \approx 1500$ K in three hours. Irradiation of helium damages the tungsten surface by forming sub-micrometer-sized structures, or fuzz [39]. The effect of pulsed plasmas to the fuzz surface was investigated. An overview of the experiments done one the targets is shown in table 5.1.

The temperature evolution of sample 1 and sample 3 during a plasma shot is shown in figure 5.1a. The steady-state temperature evolution is behaving similar for both samples, indicating

Table 5.1: Overview of the results obtained with the pulsed plasma experiments on fuzz samples

Sample properties	Sample 1	Sample 2	Sample 3
Surface material	Polished tungsten	Fuzzy tungsten	Fuzzy tungsten
Helium fluence in NAGDIS (ions)	0	10^{26}	10^{26}
Pulses in Magnum (pulses of 380-600 J of stored energy)	81	28	47
Emissivity	0.05-0.24	0.8	0.8
Damage observed	None	Slightly melted nanostructures	Melted nanostructures

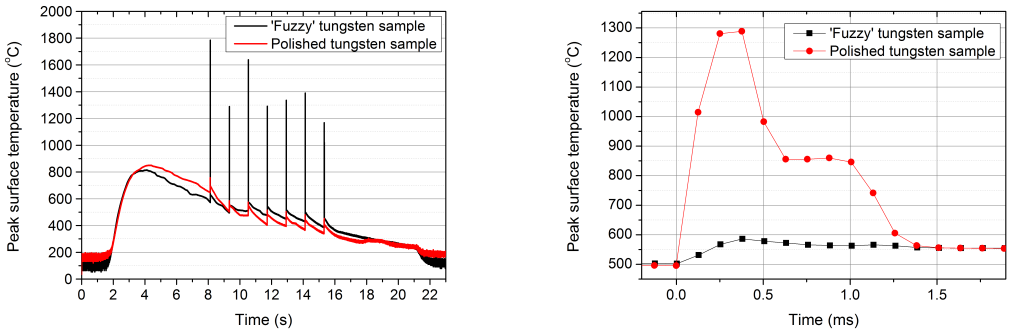

(a) (b)

Figure 5.1: Comparison of the temperature response to pulsed plasma exposure for a fuzz target and a polished target. (a) Temperature trace during a plasma exposure with simultaneous steady-state and pulse plasmas (600 J pulses) for fuzzy sample 3 and polished tungsten sample 1. (b) The 2^{nd} pulse of the plasma shots from (a) shown in more detail. Although the steady-state temperature evolution of the surface is approximately similar, the temperature increase due to a plasma pulse is much larger for a fuzzy sample.

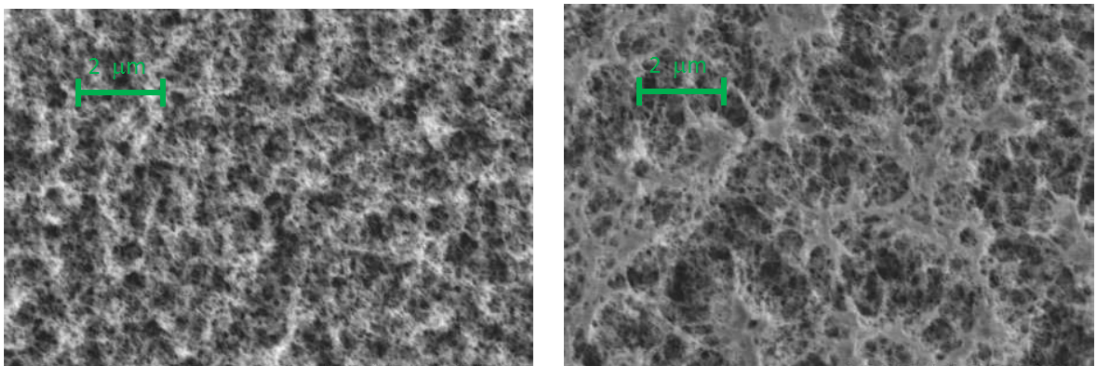

(a) (b)

Figure 5.2: The surface modifications due to pulsed plasma exposure, shown by a comparison of the edge and centre of the fuzzy target. (a) SEM image of the edge region of sample 3 exposed only to He-fluence creating the fuzz. (b) Centre of the sample exposed to both He-fluence and simultaneous steady-state and pulsed hydrogen plasma. Melting of the fuzz is shown in the centre, whereas this is not observed in the edge.

that the emissivity taken into account for the analysis of temperature is approximately correct. The decay in steady-state temperature after 4 seconds is due the magnetic field strength reducing over time. This is due to the magnetic coils heating up over time when the magnetic field is switched on. The temperature response during a plasma pulse is, however, very different. While for the polished target an temperature increase of 105 ± 11 °C was observed, the surface temperature of the fuzz target was measured to rise 915 ± 159 °C. Two mechanisms play a role in the different temperature increases to the target. First, the particle reflection coefficient at the target is much lower compared to polished targets due to the voids that are present at the nano-structures on the target surface. The particles that are reflected will likely not do so in de direction of the beam due to the roughness of the surface. Because less reflected particles will be re-ionized the plasma will be cooled down less and the electron temperature close to the target will be higher, leading to a larger heat flux to the target. Second, it is assumed that the thermal conductivity at the target surface is strongly reduced due to the fuzz [40]. When the heat flux to the surface is transiently increased, the conduction of this heat to the bulk is less compared to polished tungsten. This will greatly increase the temperature during the plasma pulse.

To see the effect of the pulsed plasma on the fuzz, the damage after pulsed plasma exposure is compared to a fuzzy region not exposed to pulsed plasmas. For each sample, the edge region of the target which was solely exposed to the helium flux in NAGDIS-II was compared with the centre region of the target which had been exposed to the helium flux and the combined steady-state/pulsed hydrogen plasma in Magnum-PSI. The damage observed with SEM images taken at the Nagoya University is summarized in table 5.1. For sample 1, the temperature increase during a plasma pulse was ∼100 °C, in line with other experiments performed on polished targets with similar settings of the pulsed plasma system. After 88 pulses, no damage was observed. Sample 2 showed slight melting on some of the nano-structures after 28 plasma pulses, while sample 3 showed clearer melting on the nano-structures after 47 pulses as shown in figure 5.2. This result is surprising, as the maximum temperature observed with the IR-Camera is ∼1800 °C whereas the melting temperature of tungsten is 3422 °C. This suggests that on nanometre scale hot spots were created that locally raised the temperature of tungsten above the melting temperature. Enhanced vaporization and ablation of tungsten of the fuzzy samples was also observed with

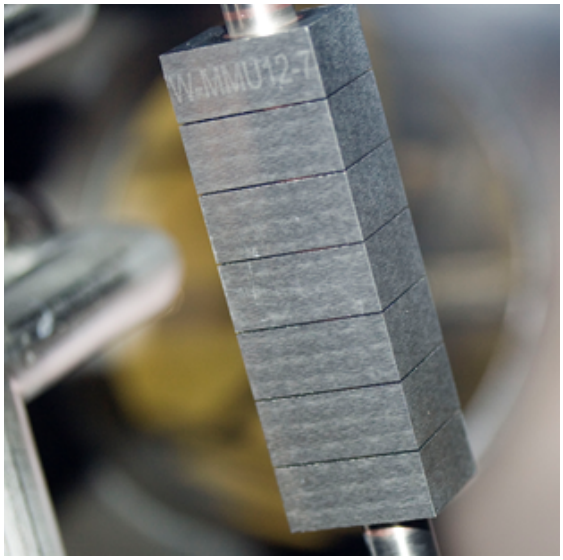

Figure 5.3: The ITER monoblocks installed in the target holder in Magnum-PSI. The ITER monoblocks consist of an array of 7 tungsten tiles, each $12 \times 21 \times 28$ mm large. The tiles are connected with a copper tube providing cooling water at $\sim$25 °C. The picture was taken before plasma exposure.

pulsed laser ELM simulations in NAGDIS-II [16]. The helium and deuterium flux that will be the exhaust products in ITER could also produce these nano-structures on the divertor surface. The extreme temperature increase that could be the result of type-I ELMs on this surface and the subsequent ablation or melting of tungsten could pose a serious risk on the plasma performance.

5.2 Recrystallization analysis of ITER monoblocks

Besides looking at the response to simultaneous steady-state and pulsed plasma exposure to different kinds of flat tungsten disks, Magnum-PSI also has the ability to test actual plasma facing components designed for tokamaks. One of the critical design issues in ITER is the divertor tiles in the plasma wetted area. These components likely receive the largest heat/particle flux and should therefore have maximal power handling capabilities through thermal conduction and provide minimal impurities to the plasma during the life-time of ITER. Therefore, a divertor consisting of tungsten monoblocks is currently planned to be installed in ITER [5]. Magnum-PSI is therefore an ideal test-bed to investigate the high heat flux performance of these components and the deterioration with both steady-state plasma and ELM-like events. The proposed monoblock design, provided by The Plansee Group, is currently being tested in three high flux test facilities: JUDITH 2 in Forschungszentrum Julich, GLADIS in IPP Garching, and Magnum-PSI. The monoblock installed in Magnum-PSI is shown in figure 5.3.

The motivation for these experiments is to assess the behaviour of tungsten near or above the recrystallization temperature, $\sim$1300 °C for this grade of tungsten, in combination with transient temperature pulses. The change in material properties is evaluated over a large amount of ELM-like pulses and large hydrogen fluence; 17400 pulses and $> 10^{28}$ m^{-2}, respectively for this experiment. This is the equivalent of more than three 10 minute plasma discharges in ITER, assuming type-I ELMs with a frequency of 10 Hz. The heat flux to the monoblocks was monitored

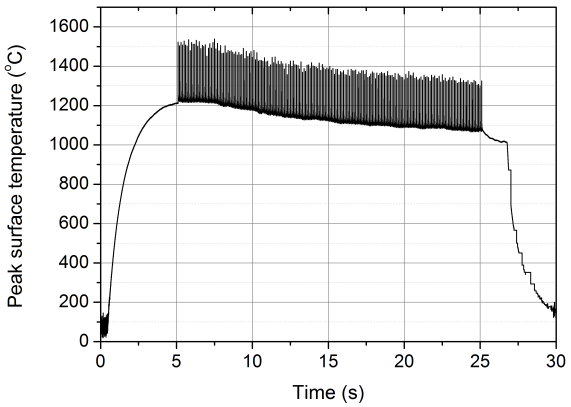

Figure 5.4: Peak surface temperature evolution over time due to combined steady-state and pulsed plasma exposure. The settings used during this shot were 5.4 slm of injected hydrogen gas with 225-235 A of steady-state current, and plasma pulses with 60 J of stored energy with 10 Hz in B-field setting 2. To adjust for the lower steady-state flux due to the magnetic copper coils heating up, as observed in figure 5.1a, the steady-state arc current in the source was increased by 0.5 A/s.

during the experiment, while the change in material properties will be evaluated by the ITER organization. This experiment is the first in a set of experiments on these monoblocks to assess the effect of recrystallization on the high heat flux performance of tungsten. More experiments are planned.

As shown in section 4.2.1, inserting a target further into the linear magnetic field strongly increases the heat flux to the target. To obtain the temperatures as required for the ITER monoblock experiments, the target was inserted 98 mm further compared to the general measurement position into the magnetic field, 80 mm away from the Thomson scattering position. This position inhibits Thomson scattering measurements, but with an additional mirror placed in the vacuum vessel it is possible to monitor the target surface with the IR-Camera. The temperature evolution of the surface is shown in figure 5.4. In this shot, after 9800 plasma pulses, $T_{base} \approx 1150$ °C was found with 1.2 ms pulses at the target that increase the temperature by 238±17 °C. From THEODOR, the corresponding peak heat and energy flux are 175 MWm^{-2} and 94 kJm^{-2}, respectively.

For the ITER monoblocks it is crucial that the thermal conductivity of the material does not deteriorate over time due to periodic recrystallization events. Worsened power handling will imply that heat is transferred more slowly to the cooling water which can lead to an increased surface temperature for a given heat flux. The temperature increase during an ELM, which is due to the sudden increase of heat flux to the target, is therefore a first indicator of power handling deterioration.

The temperature increase, ΔT_{pulse}, for several shots and the corresponding total number of ELM-like events that have occurred before that shot is shown in figure 5.5. It shows that ΔT_{pulse} actually decreases slightly after approximately 6500 plasma pulses from ΔT_{pulse}=265°C to ΔT_{pulse}=230°C. One of the possible explanations for this decrease is that by having many transient recrystallization events near the surface, the power handling of the tungsten tile actually improves. The grain structure of tungsten at the surface would then have rearranged to improve

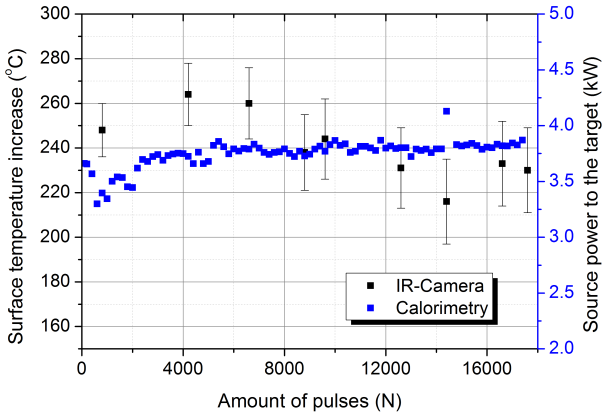

Figure 5.5: A first indication of the change in thermal properties of the ITER monoblocks through pulsed plasma exposure. The temperature increase is shown here as a function of number of pulses received by the monoblock. This is compared with the power deposited to the target as measured from calorimetry. In total the monoblock was exposed to 17400 pulses during 88 plasma shots. A decrease in ΔT is observed after approximately 6500 pulses, while the power from the source remains constant throughout the experiment.

the heat conduction of these transient heat flux increases. The risk of recrystallization is that the binding of grains at the surface can become weak, which could result into microparticles of tungsten ending up more easily in the plasma during disruptions in a tokamak. To ensure that the drop in ΔT_{pulse} is not caused by deterioration of the source, the average power conducted to the cooling water during a shot is also plotted in figure 5.5. Apart from the first 2000 pulses, the source output appears constant. For the first 2000 pulses, the lower average power to the target can be attributed to a change in input parameters. Here, the steady-state current was increased with 0.5 A/s throughout the shot to compensate for the weakening B-field strength due to the magnetic coils heating up, as discussed for figure 5.1a.

Although the monoblocks will be analysed *post-mortem* by the ITER organisation, some initial effects on the source can be observed by eye. Throughout the experiment, the plasma wetted surface on the tungsten tile started to appear whiter compared to the non-wetted surface, as shown in figure 5.6. This also suggests that the surface is modified due to the plasma pulses. The increase in emissivity of the affected surface is shown in figure 5.7. Here, the digital level at the spot, measured with IR-Camera was compared between several shots to the measured digital level before exposure. The emissivity starts to increase after approximately 8000 pulses, which is in agreement with the increased power handling as shown in figure 5.5. This data suggest that there is roughening near the target surface which could be explained by the large thermal cycling and the resulting stresses on the surface, although this will have to be confirmed by SEM analysis later. It is also unsure what the effect of this surface modification will be on the divertor in ITER.

This experiment shows that the pulsed plasma system in Magnum-PSI is able to test the effects of extreme plasmas on tokamak components for a large ion fluence and a large number of plasma pulses. Although limited by the magnetic field, the heat flux to the target can be significantly increased by inserting the target further towards the linear B-field. It is expected that with the superconducting magnet, larger numbers of ELMs can be simulated in one shot,

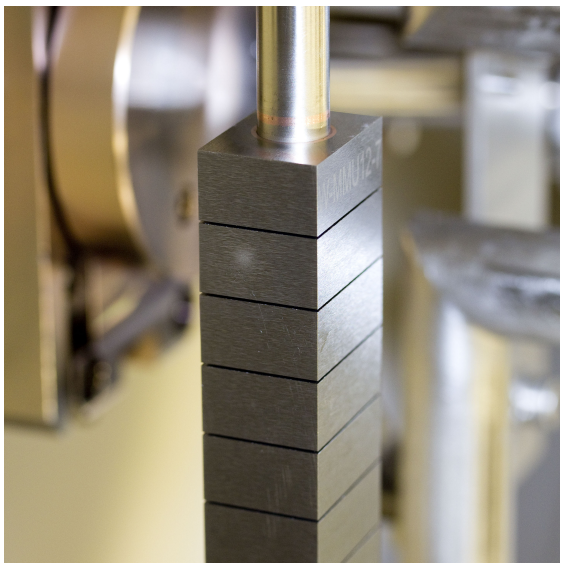

Figure 5.6: Photograph of the ITER-monoblocks after exposure to 17400 plasma pulses and 88 shots in Magnum-PSI. The plasma-wetted tile shows a white spot indicating an increase of emissivity.

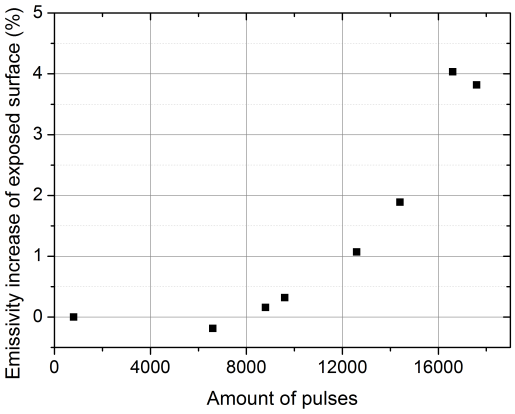

Figure 5.7: The emissivity change at ∼25°C as measured with the IR-Camera at the centre of the white spot shown in figure 5.6. The increase in emissivity is found by comparing the digital levels of IR-Camera images taken at room temperature between shots. The centre of the plasma wetted area on the target is compared with an IR-image taken before plasma exposure. The emissivity starts to increase after 8000 pulses.

and higher heat fluxes can be obtained. This is, however, the very first time that plasma loading with simultaneous steady-state and pulsed plasmas is realized on such long time scales. In the future, more experiments on the monoblocks with base temperatures above the recrystallization temperature and even transient melting experiments are foreseen.

5.3 Shallow-melting of tungsten due to transients in Pilot-PSI

Another concern for the divertor in ITER is the effect of melting due to transient events on tungsten. This could be either due to disruptions in the plasma or even due to unmitigated type-I ELMs. Transient melting could result into mobilization of the melt layer due to various forces on the divertor material. Repeated melting could furthermore lead to damage to the PFCs, by embrittlement or reduced thermal conductivity, or erode the material away [41]. In this experiment, these effects were investigated by increasing the temperature of tungsten above the melting point during a plasma pulse; the so-called *shallow melting*. First, the amount of melted material and the implications for ITER were investigated as a function of pulse number. Second, droplet ejection and layer stability during a shallow melting event was investigated.

Because the heat flux to reach melting is limited by the magnetic field strength in Magnum-PSI, the pulsed plasma system in Pilot-PSI was used in the shallow melting experiments. In the pulsed plasma system of Pilot-PSI, heat fluxes of > 1 GWm^{-2} can be obtained, i.e. 6 times higher than is presently possible in Magnum-PSI and in the range that is expected for type-I ELMs in ITER. This system is based on the same principle: an array of capacitors is discharged in the plasma with simultaneous steady-state plasma [42]. The electronic design is, however, different which implies that the pulse duration, $\sim$1.3 ms, in Pilot-PSI is fixed regardless of input energy. The results obtained from the pulsed plasma in Pilot-PSI were furthermore compared to shallow melting experiments done with ELM simulation using pulsed lasers in Magnum-PSI by G.G. van Eden [41].

The high speed visible camera with a W-I filter mounted perpendicular to the target to monitor splashing and evaporation. The surface temperature was measured with the fast IR-Camera, while the emissivity was calibrated with the pyrometer. The settings of the pulsed plasma system were optimized to achieve the maximum temperature increase. All experiments were performed with $B_{target} \approx 1.6$ T with 10 slm of hydrogen gas injected and pulses with $\sim$560 J of dissipated energy in the plasma during a plasma pulse. To achieve the high steady-state temperatures, 1 mm thick tungsten disks were insulated from the cooling water with an additional tungsten disk and grafoil on the back-side of the target. The samples were analysed *post-mortem* both optically and with SEM. The latter analysis was done in collaboration with the Institute for Plasma Physics in the Czech Republic.

A typical temperature trace for the shallow melting experiments is shown in figure 5.8. Here, the base temperature is increased to approximately 3000°C in steady-state, while heat flux due the plasma pulse increases the surface temperature with approximately 800°C. This is above the melting temperature of tungsten, which is 3422°C. The peak heat flux to the target was approximately 0.8 GWm^{-2} with an energy flux of 0.4 MJm^{-2} for a 1.3 ms pulse. To quantify the effect of multiple shallow-melting events, several samples were exposed to a different number of plasma pulses. An overview of the results is shown in table 5.2.

The photographs of the targets are shown in figure 5.9. Sample 1, which was exposed to one plasma pulse shows no signs of a melt pool. The plasma wetted area on the target does, however, show roughening due to recrystallization. Sample 4 and sample 2 do show a melt pool in the centre of the roughened plasma wetted area. This indicates that in the centre of the plasma beam, the surface temperature was raised above the melting temperature of tungsten

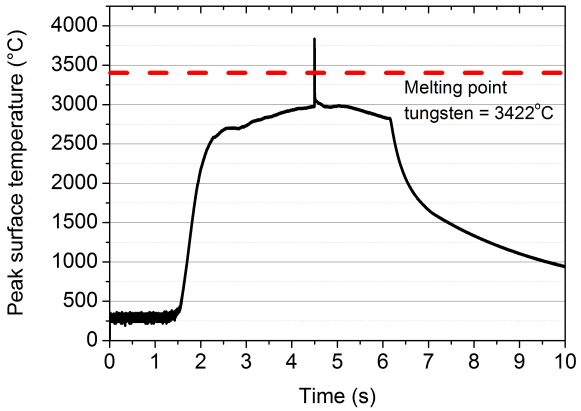

Figure 5.8: The temperature evolution of the surface of a tungsten target during the shallow-melting experiments. A steady-state temperature of 3000°C was achieved due to bad thermal contact between that target and the cooling water. The surface temperature is increased with approximately 800°C to 3800°C, ∼400°C above the melting temperature of tungsten.

Table 5.2: Overview of the samples exposed and results obtained during the shallow melting experiments in Pilot-PSI.

Sample properties	Sample 1	Sample 2	Sample 3	Sample 4
Hydrogen fluence to the target (ions/m^2)	8×10^{24}	$1.6{\times}10^{25}$	8×10^{24}	$3.2{\times}10^{25}$
Number of pulses	1	15	1	4
Melt pool observed?	No	Yes	No	Yes
Diameter of melt spot	-	5.2 mm	-	2.8 mm

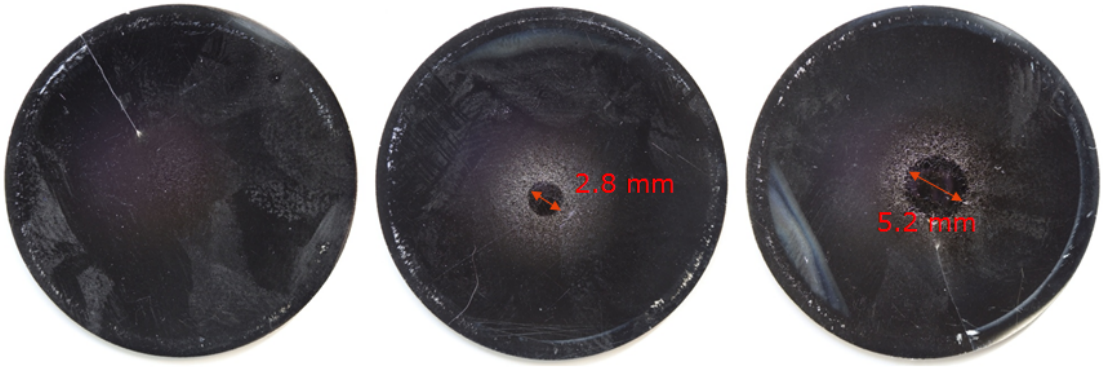

Figure 5.9: The exposed targets photographed showing a first indication of shallow melting. From left to right, sample 1, 4, and 2 are shown. The targets were exposed to 1, 4, and 15 plasma pulses, respectively. Whereas only roughening in the centre at the position of the beam axis is observed, a melt spot can be seen for the targets exposed to multiple transient melting events.

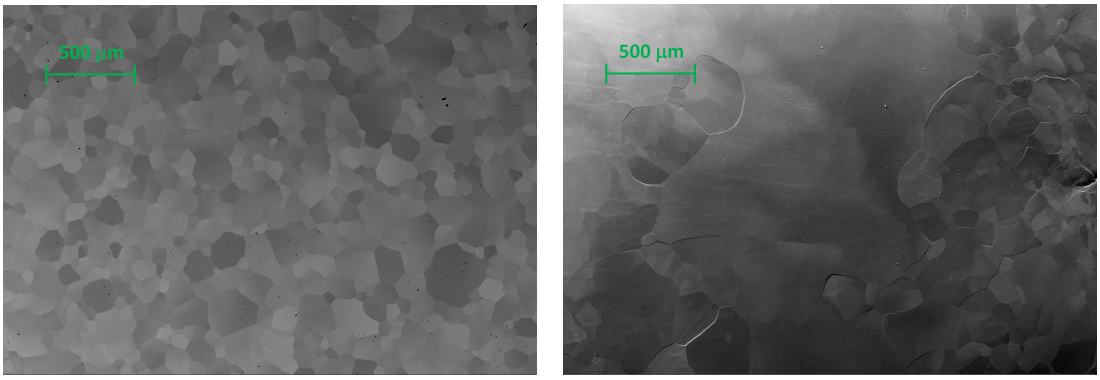

(a) (b)

Figure 5.10: SEM images of the centre of the plasma wetted area. (a) Sample 1, which received one pulse, and (b) sample 2, which received 15 pulses, are shown here at similar scale. Grain growth is observed for sample 1 up to 60 μm in diameter. For multiple pulses, the grain size increases significantly up to 1 mm.

for a sufficiently long time to create a melt spot. The diameter of the melt pool is 2.8 mm for sample 4 and 5.2 mm for sample 2, suggesting a progressive increase of the melted material as a function of plasma pulse number.

The grain evolution is analysed in more detail from SEM images of the surface as shown in figure 5.10. In this figure the centre of the plasma wetted area is shown for the roughened surface of sample 1 and the melt pool of sample 2. Here it is shown that the grains grow in the centre of the plasma to 60 μm in diameter after one plasma pulse for sample 1 compared to 10-15 μm which is the original grain size. In sample 2, after 15 pulses, extremely large grains of up to 1 mm in diameter are observed.

An overview of the average grain sizes in the centre of the spot as a function of pulse number is shown in figure 5.11. The results are obtained from the SEM images of the samples and were compared with the samples that were created from shallow melting experiments using simultaneous steady-state plasma with pulsed lasers. Here, it is shown that for a single plasma pulse the average grain size increases from 10-15 μm to approximately 60 μm, corresponding with grain growth at the surface shown in sample 1. This effect was also observed for the pulsed laser experiments with 30 and 120 laser pulses. The difference between pulsed laser and pulsed plasma, however, is shown for multiple pulses. The average grain size is strongly increased for multiple pulses from the pulsed plasma compared to the constant grain size as a function of pulses from the laser. The mechanism that could explain the difference between both experiments is the steady-state temperature for the pulsed plasma that was much higher compared to the pulsed laser, 2700-3000°C compared to 1500°C. The total duration of the larger steady-state temperature was also much larger as only one plasma pulse per plasma shot can be generated in Pilot-PSI. The strong recrystallization during the pulsed plasma experiments for a relatively long time duration could therefore enhance the size of the grains. This is not observed for the samples exposed to a single pulse during one plasma shot. For the samples exposed to one plasma shot, however, the duration of the increased steady-state temperature was similar to the duration of steady-state plasma exposure for the two samples exposed to simultaneous laser pulses.

To investigate the effect of the depth of the melting layer, the samples were cleaved through the centre of the melting affected area and SEM images were taken of this cleaved area. These

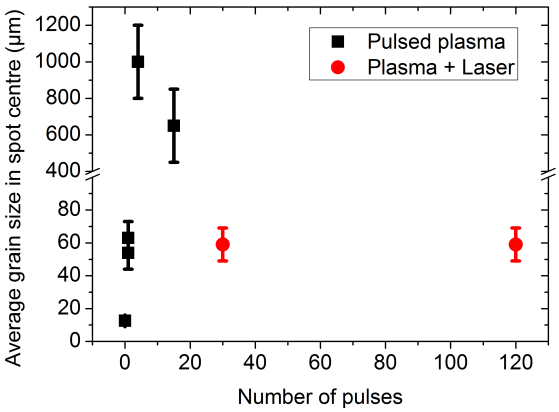

Figure 5.11: The average grain size as created with pulsed plasmas compared with the average grain size found for the shallow melting experiments with pulsed lasers. The average grain size in the centre of the plasma wetted area is shown as a function of number of transient melting events. Although the grain size did not increase in the pulsed laser experiments, significant growth is observed for pulsed plasma exposure for far less pulses.

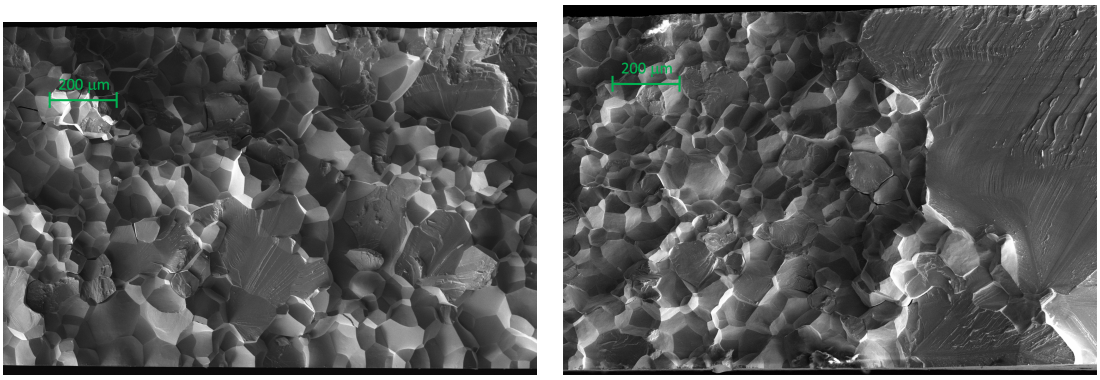

(a) (b)

Figure 5.12: Investigation of the depth of the melt layer from SEM images of a cross-section of samples through the centre of the melt spots. (a) The centre of the recrystallized spot of sample 1 and (b) the edge of the melt pool of sample 4. In both cases recrystallization is observed over the entire thickness of the samples.

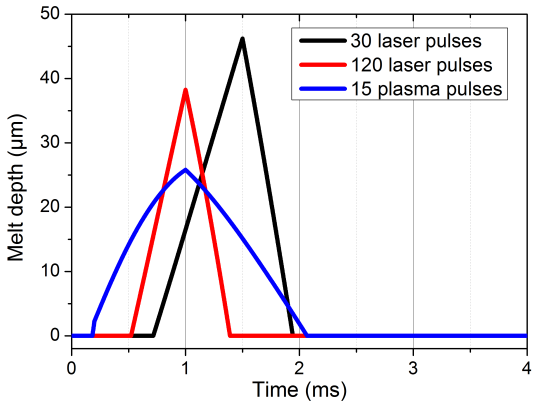

Figure 5.13: Calculated melting depth evolution during a shot for laser pulses and plasma pulses over time. Two different laser pulse settings with peak heat flux of approximately 1.35 GWm−2 and a pulse duration of 1 ms and 1.5 ms were used for the 120 and 30 laser pulse samples, respectively. The different temperature profiles were used as an input for the calculations. The calculations show that the melting depth is expected to be smaller for the plasma pulses, although this was not observed in the SEM images.

SEM images are shown in figure 5.12. Here, an enlargement of the grains due to recrystallization is observed for sample 1, while clear signs of melting are not observed. The recrystallization was observed throughout the entire depth of the target. For sample 4 the melt area, which contains significantly larger grains, is seen throughout the depth of the 1 mm target. There is furthermore a clear step-like transition at the edge of the melt pool between the large grain in the melt pool and the recrystallized grains in the edge, which have an approximately similar diameter as the grains observed in sample 1. These results imply that the exposure time was long enough during a single exposure for recrystallization to take place throughout the sample during steady-state exposure, not simply during the plasma pulse, due to the much elevated steady-state temperature. The enlarged grain size for multiple pulses could be explained by the subsequent growth of grains starting with an increased diameter after each plasma shot.

The expected thickness of the melt-layer, d_m, for a known surface temperature over time can be calculated from [43]

$$d_m(t) = 2\lambda\sqrt{\alpha_m t}, \tag{5.1}$$

where α_m is the thermal diffusivity of the melted material and λ is a numerical constant. λ can be determined from

$$\frac{\lambda L\sqrt{\pi}}{c_m(T_s(t)-T_m)} = \frac{e^{-\lambda^2}}{\mathrm{erf}(\lambda)} - \frac{K_s\sqrt{\alpha_m}T_m e^{-\frac{\lambda^2\alpha_m}{\alpha_s}}}{K_m\sqrt{\alpha_s}(T_s(t)-T_m)\mathrm{erf}(\lambda\sqrt{\frac{\alpha_m}{\alpha_s}})}, \tag{5.2}$$

where L is the heat of solidification, and c, K and α are the heat capacitance, thermal conductivity, and thermal diffusivity, respectively, for solid (s) and melted (m) tungsten. The calculated evolution of the melting depth for the known surface temperature evolution, measured with the IR-Camera, is shown in figure 5.13. The melting depth due to a laser pulse is calculated to be 36-45 μm while this is 25 μm for the plasma pulse. This is attributed to the top-hat heat

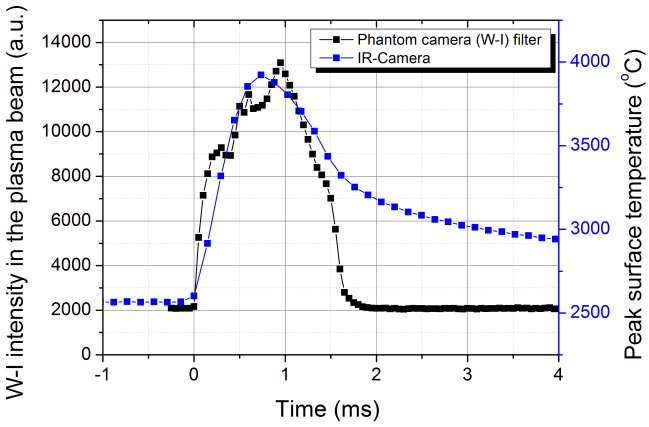

Figure 5.14: Investigation of evaporation of tungsten during a transient melting event. The integrated evolution of the tungsten-I line emission in the plasma beam, measured with a fast visible camera, is shown here. The results are compared to the peak surface temperature evolution on the surface. During the pulse, tungsten was evaporated in the plasma.

flux of the pulsed laser, which heats the target surface for a longer duration with higher heat flux. The calculated depth is much smaller than the 1 mm thickness observed experimentally. This suggests that the effect of recrystallization in the tungsten bulk due to the steady-state temperature plays a large role on the depth of the melt layer.

With a fast visible camera placed perpendicular to the target, the tungsten erosion from the target to the plasma was measured. During the first plasma pulse to a target, ejected particles were observed from the surface. These particles were most likely loosely bound particles or dust on the surface because no other ejected particles were observed to come from the surface after the first pulse. Splashing of the melted particles during a pulse was not observed. Tungsten evaporation was observed with a W-I filter in front of the target during a plasma pulse, as shown in figure 5.14. The increased plasma pressure due to the evaporation cloud in front of the target could drive the motion of the melted material radially outside from the centre of the beam, as was observed for sample 2, exposed to 15 plasma pulses.

The shallow melting experiments show that the amount of melted material due to transient melting can be large in the current plasma conditions. Because the depth of the melting layer was larger than the thickness of the tungsten disks, similar experiments should be performed on thicker tungsten samples to see what the actual depth is. The large grains formed at the surface can cause embrittlement of the surface which implies that these large grains could end up in the plasma more easily. This could be a concern for the ITER divertor if these conditions were reached. It is, however, not expected that a T_{base} of 2700-3000°C and the associated grain growth will be reached in ITER. The motion of the melted layer due to plasma pressure, as found in sample 2, could be of concern to the ITER divertor. Because the divertor tiles are placed under a sharp angle with the incoming plasma to spread the power load to the surface, it is possible that irregularities on the surface will quickly be eroded due to the strongly increased heat and particle flux on this position.

The results found from the pulse plasma system could furthermore serve as a benchmark for shallow melting experiments which will be performed in JET in the summer of 2013.

Chapter 6

Summary and suggestions for further research

6.1 Summary of this thesis

The goal of the experiments presented here was to investigate the effect of ITER-like ELMs in combination with a steady-state ITER-like plasma flux on tungsten targets. The energy flux of these ELMs is expected to be approximately 1-10 MJm^{-2}. The experiments were mainly performed on a novel setup designed to replicate periodic ELMs by plasma pulses in Magnum-PSI. To answer the research question stated in the introduction, *What is the effect of periodic ITER-like ELMs with simultaneous steady-state plasma on tungsten targets?*, the research was split up in three part. First, the pulsed plasma system in Magnum-PSI was characterized. Here, the relationship between the input parameters and the plasma response in terms of dissipated power, impedance, electron temperature and electron density was investigated, and the operational range of the system was determined. The main input parameter of interest was the amount of energy dissipated per pulse. After this part, the question, *How can ITER-like ELMs be simulated?*, should be answered. Second, the effect of the increased plasma parameters on the heat flux to the target was investigated. The question addressed here is: *What is the response of the target to transiently increased plasma parameters during a plasma pulse?* Finally, several experiments on tungsten targets were performed, addressing questions relevant for the design of the divertor of ITER: *What will the impact of ELMs be on plasma-facing components in the ITER divertor?*

The pulsed plasma system in Magnum-PSI has been successfully commissioned and represents a major upgrade of the single-pulse Pilot-PSI system. The electron temperature and electron density were increased through Ohmic heating throughout the plasma beam by discharging the stored energy in the capacitor bank in the plasma. Furthermore, the time evolution of the power dissipated in the plasma beam resembles the shape and pulse duration as expected for type-I ELMs in the ITER divertor.

The power dissipation in the plasma beam was shown to increase with input energy. The increase of power was attributed to the change in voltage between the cathode and anode of the plasma source, which is indirectly controlled by changing the charging voltage of the capacitors, and to the change in resistance of the plasma. When the pulse is changing from resonance mode to decay mode, the voltage across the capacitors is zero and the peak power dissipated is therefore solely determined by the plasma resistance across the current path of the electrons. The plasma resistance is observed to decrease during a plasma pulse which is consistent with

the measured increasing electron temperature in the plasma beam. For stored pulse energies > 200 J, the electron temperature does not increase with pulse energy, and therefore the change of peak power with pulse energy is also reduced. The change of inductance in the plasma beam was found to be negligible compared to the effect due the change in plasma resistance during the pulse.

The peak electron temperature near the target was observed to stop increasing for pulse energies > 200 J. During the experiments it was possible to measure the evolution of electron temperature and electron density during a plasma pulse through single-shot Thomson scattering. These measurements were done close to the target, $\sim$1 m away from the source. It is expected that the temperatures measured at this positions are lower compared to the temperatures in the linear magnetic field, where most of the power is dissipated, due to a small amount of electron current arriving to the target.

It was shown that the gas is fully ionized for pulse energies of > 30 J. The peak electron density decreases near the target for pulse energies > 200 J. The drop in peak electron density was attributed to the increased velocity of ions leaving the source for higher electron temperature. This leads to lower electron densities due to the limited particle flux when the gas is fully ionized. For low electron density, the plasma is likely too cool down more quickly along the plasma beam due to the increased interaction with neutral particles along the beam. Therefore, there is a balance between electron temperature and density that limits the range of plasma parameters obtained in the pulsed plasma system.

The range of peak plasma parameters found for these experiments with B-field setting 3 near the target were $n_e = 6.8 - 12 \times 10^{20}$ m^{-3} and $T_e = 2.8 - 6.8$ eV. These are significantly lower compared to the values obtained with Pilot-PSI, ranging to $T_e = 12$ eV and $n_e = 50 \times 10^{20}$ m^{-3}. It was found that this is due to the diverging B-field of Magnum-PSI near the target, which is typically a factor 5-7 lower near the target compared to the linear B-field. The linear B-field would result in a strongly confined beam with higher electron density and less cooling along the axial direction of the beam. The factor 5-7 drop in B-field is consistent with the factor $\sim$5 of higher peak electron density found in Pilot-PSI. To answer the first research question: The settings yielding maximum electron density and temperature are for plasma pulses with stored energy of 60-120 J. A linear B-field close to the target is, however, needed to achieve the heat and energy fluxes necessary to replicate ITER-like ELMs.

To address the second research question: The main effect that can be observed experimentally during the measurement on the target as a response to these increased plasma parameters is an increase of surface temperature. The surface response was measured with a fast IR-Camera, measuring the temperature evolution of the surface. From the temperature evolution, heat flux and energy flux were calculated using THEODOR. Varying the stored energy of the plasma pulses, it was observed that ΔT_{pulse} of the surface decreased for an increase of pulse energy, corresponding to less heat flux arriving at the target. The decrease in peak heat flux found with the IR-Camera were in line with the plasma parameters found with Thomson scattering. Peak heat fluxes to the target were found to range between 142 and 180 MWm^{-2} with a corresponding energy flux between 20 and 60 kJm^{-2}. These values are not high enough to replicate type-I ELMs expected in ITER and their associated damage, but do allow for the testing of other properties of interest for the design of the ITER divertor. When extrapolating the measured effects of the linear B-field with higher magnetic field strength, it is expected that the values expected for ITER will be achieved.

Finally, some of the applications of the pulsed plasma system of both Magnum-PSI and Pilot-PSI were shown and the implications for ITER were discussed. It was found that for fuzzy tungsten samples, having nanostructures on the target surface due to helium irradiation, the peak temperature increase was much larger compared to the temperature increase on polished

tungsten targets. The strong increase of surface temperature even led to local melting of some of the nanostructures. This poses a large risk for the divertor in ITER because the loosely bound nanostructures could end up in the divertor. This could lead to tungsten impurities ending up in the plasma. The creation of fuzz on the tungsten divertor surface should therefore be prevented in ITER. The energy fluxes here are relatively low, and the melting effects due to higher energy fluxes could be worse.

ITER monoblocks were successfully subjected to longevity studies of transient recrystallization events due to the pulsed plasma. For this experiment, an ITER monoblock was exposed 17400 pulses with 96 kJm^{-2}, while the base temperature was just below recrystallization at $\sim$1150°C. After approximately 8000 pulses an improvement in power handling was observed which could be due to recrystallization. This could, however, also increase the chance of embrittlement of the monoblock. The experiments on this are ongoing, and the effect of the material properties will be analysed in more detail *post-mortem* by the ITER organisation.

In the last set of experiments described in this thesis, the shallow melting effects of tungsten were investigated. Here, the mobility of the melted layer and the amount of melted material due to transient melting events was analysed. These experiments were performed in Pilot-PSI, where heat fluxes of > 1 GWm^{-2} can be obtained, i.e. 6 times higher than is presently possible in Magnum-PSI and in the range that is expected for type-I ELMs in ITER. For multiple pulses, strong recrystallization was observed which could be due to melting. The melt spot was found to be growing as a function of number of transient melting events. The depth of the recrystallized layer was observed to be larger than 1 mm. The generation of these large grains should be prevented in ITER as they could lead to embrittlement of the divertor. Although evaporation around the target was observed, no particle ejection or splashing of the melted material was observed.

In the context of ELM replication experiments, it was shown that the interaction between tungsten targets and the pulsed plasmas on top of a steady-state plasma was different compared to ELM replication with pulsed lasers [41]. During the shallow melting experiments which were done with pulsed laser and pulsed plasmas, an increase of damage due to pulsed plasmas was observed.

Characterizing the pulsed plasma system in Magnum-PSI confirms that the conditions created during ELM simulations are different from other ELM replication methods. Plasma guns [18] can generate transient heat loads and ion energies relevant for ELM simulations, but lack the steady-state plasma load in between these transient event. The electron beam facility JUDITH [44] is able to provide relevant energy fluxes, but lacks the plasma environment. Pulsed laser experiments in combination with steady-state plasmas in linear plasma generators [17, 16, 41] are a suitable candidate for ELM replications, as they provide extreme flexibility in repetition rate, pulse duration and peak heat flux. These do, however, still not replicate the transiently increased plasma density and corresponding particle flux to the target. As the plasma conditions generated during a plasma pulse with simultaneous steady-state plasma do resemble an ELM-like event very well, Magnum-PSI and the pulsed plasma system will likely serve as an important facility in testing components of the ITER divertor design.

6.2 Further steps for the pulsed plasma setup in Magnum-PSI

In this thesis, the general properties of the pulsed plasma system were investigated and the effect of the pulsed plasmas on tungsten targets was presented. The type-I ELM conditions as expected for ITER, however, have not yet been reached. With the current setup, achieving these conditions is not possible. It was shown that for a linear magnetic field near the target,

the heat flux to the target increases, and it is expected that with the superconducting magnet the required conditions will be reached. This was also shown with the pulsed plasma system in Pilot-PSI, which is able to generate peak heat fluxes of approximately 1.5 GWm^{-2}.

Due to possibility of retracting the target and obtaining high frequency plasma pulses, some other effects could be investigated if higher heat fluxes were obtained in Magnum-PSI. It was suggested by J. Zielinski [24] that for these high particle and heat fluxes the target would 'shield' itself by the transient release of hydrogen particles trapped in the superficial surface. This effect, which would be good news for the ITER divertor, could be validated in Magnum-PSI by varying the pulsing frequency. In this way, the number of hydrogen particles that are trapped in between pulses could be reduced by increasing the pulse frequency which would eliminate the self-shielding effect. Alternatively, the effect of the reflected particles could be investigated by retracting the target, similar to the method used in section 3.3.

As an intermediate solution, the pulsed plasma system could be connected to the plasma source in Pilot-PSI. Here it could be validated that ITER-like energy fluxes are indeed observed. Through a frequency scan, *self-shielding* could be investigated. It would furthermore allow for experiments which require repetitive plasma pulses with high heat fluxes, such as the shallow melting experiments. In the later case, the effect of recrystallization during the steady-state plasma would be minimized as in one shot more than 30 plasma pulses can be generated compared to 1 in the current pulsed plasma system in Pilot-PSI.

Furthermore, the effect of several ELM simulation methods should be compared more thoroughly. In Magnum-PSI, ELM simulations can be done with pulsed laser and pulsed plasma, and in JUDITH ELMs can be simulated with a scanning electron beam. By measuring the response to the target using similar heat loads, the effect of ions, photons, and electrons on a tungsten target could be compared. In this way, the impact of each particle to the exposed material could be isolated. This should further enhance the knowledge of the expected damage to the ITER divertor.

Finally, improvements to the pulsed plasma source, designed for pulsed plasma operation should be made. Throughout this thesis, several designs for the nozzle of the source were tested of which a tungsten coated (200 nm) Cu/W plate is currently the most promising design. It was shown that the design of the source has a significant impact on the plasma production and could limit the input parameters during plasma exposures. This is of importance in the reproducibility of plasma parameters as well as in longevity studies, for which the life-time of the source should be maximized. The significant improvements made here are exemplified in the realization of the first experiments on the ITER monoblocks.

6.3 Final conclusion

In this thesis, the effect of periodic ITER-like ELMs with simultaneous steady-state plasma on tungsten targets was investigated. The main research question was investigated by characterizing the pulsed plasma system and investigating the effect of these pulsed plasmas on several target.

It was shown that the pulsed plasma system is able to transiently increase the electron temperature and electron density to 6.8 eV and 12×10^{20}, respectively, for a duration of approximately 1 ms. These values are in the same range as the plasma parameters found in a divertor plasma during a type-I ELM. The shape of the time evolution of heat flux to the target due to the increased electron temperature and density is similar to the shape of the heat flux in a divertor during an ELM. It was furthermore shown that these conditions can be controlled by changing the energy discharged in the plasma during a pulse. This makes the pulsed plasma system in Magnum-PSI a suitable device to simulate ELMs which has the unique ability to combine a

steady-state plasma load with simultaneous periodical particle and heat fluxes to a wide range of target. Although the fluxes as expected in ITER during a type-I ELM are not reached, it was found that these conditions will be met when a linear B-field is present near the target. With a superconducting magnet, planned to be installed in November 2013 in Magnum-PSI, this is likely to happen in the near future.

In this thesis, the first experiments on the effects of recrystallization due to ELMs on ITER monoblocks were presented. It was possible to expose the monoblocks to 17600 plasma pulses with approximately 100 $\mathrm{kJm^{-2}}$ of energy flux per pulse. This shows that currently, long plasma exposures with simultaneous plasma pulses are possible with the pulsed plasma system in Magnum-PSI.

Appendix A

Reference graphs for Pilot-PSI and Magnum-PSI

The two linear plasma generators available at DIFFER, Pilot-PSI and Magnum-PSI, are both equipped with a system that allows for the generation of pulsed plasmas. While experiments on both systems have been discussed in this thesis, the characterization of the pulsed plasma system was done on Magnum-PSI. The characterization of the pulsed plasma system was extensively described by Jakub Zielinski [24]. This appendix will compare the output parameters of the two systems.

The electronic design of the pulsed plasma system in Pilot-PSI is shown in figure A.1. The systems consists of 56 capacitors joined in seven stacks of 1200 μF, with 7 inductors, 70 μH, coupled in parallel. There are two fundamental differences between this system and the pulsed plasma system of Magnum-PSI shown in figure 2.3. First, the capacitors in Pilot cannot be charged or discharged independently. As the typical charging time is $\sim$10 s, the capacitor can typically be discharged one time during a plasma shot. Second, the capacitors in this system can be positively and negatively charged, while in the system in Magnum only a positive charge is possible. Therefore, the system remains an RLC circuit throughout the pulse or stays in resonance mode. The resulting current curve in this system can be described by the first half of

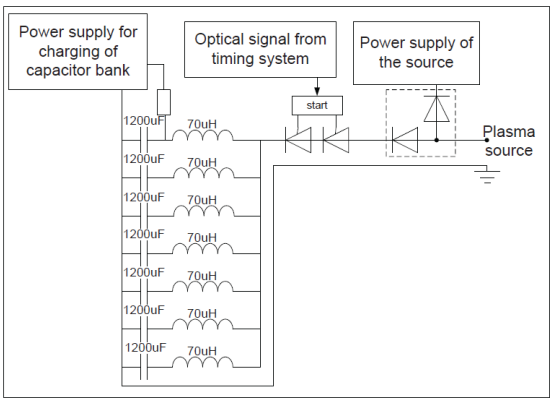

Figure A.1: Schematic view of the electric design of the pulsed plasma system in Pilot-PSI.

a sine wave,

$$I(t) = I_0 \sin(\frac{t}{\sqrt{LC}}) \quad \text{for } 0 < t < \pi\sqrt{LC}. \tag{A.1}$$

The resulting pulses typically have a duration of approximately 1.3 ms independent of the energy stored in the capacitor banks. The efficiency, $\eta = \frac{E_{dissipated}}{E_{stored}}$, was found to be 50% in Pilot-PSI. This is lower than the efficiency of ∼80% in Magnum-PSI.

During a discharge this will result in different temporal evolutions of current and voltage in the plasma as is shown in figure A.2. Whereas the voltage difference between cathode and anode is increased in resonance mode and decreased in decay mode compared to the steady-state voltage in Magnum-PSI, the voltage difference is solely increased in Pilot-PSI. The shape of the current through the plasma is furthermore more peaked in the case of a pulse in Magnum-PSI. This shape does represent the actual shape of the heat flux to the divertor in a tokamak during a type-I ELM better [30].

Because in Pilot-PSI the peak current of a pulse is typically used as a measure for the set charging voltage in the capacitors a graph of stored energy versus peak current for both Pilot and Magnum is shown in figure A.3.

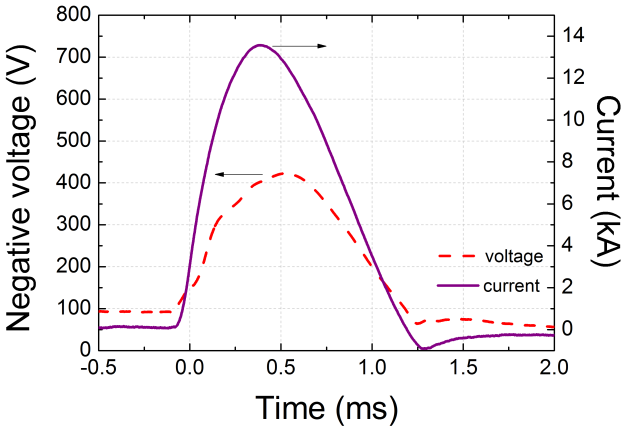

(a)

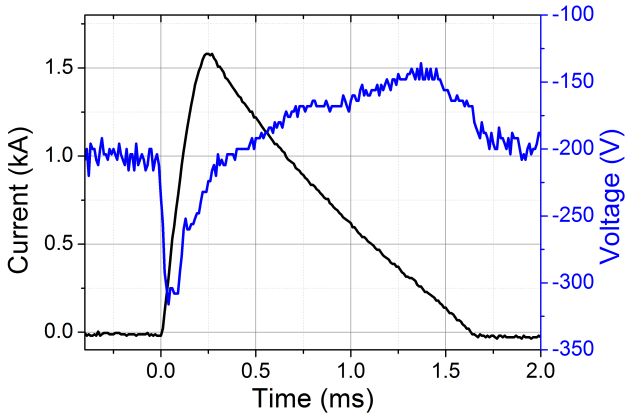

(b)

Figure A.2: Typical current and voltage traces during a plasma pulse. (a) The evolution of current and voltage in the pulsed system on Pilot-PSI [24]. The stored energy in the capacitors was in this case 4200 J. (b) The evolution during a pulse in Magnum-PSI. The stored energy was in this case 320 J.

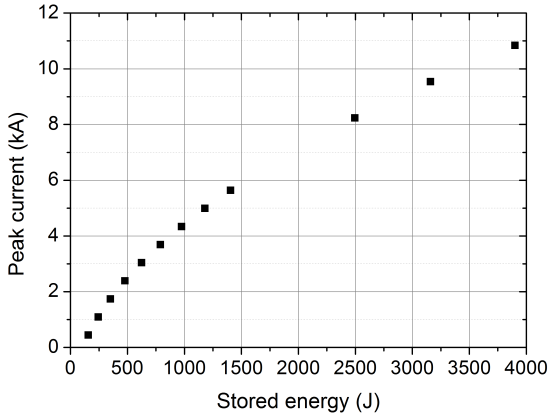

(a)

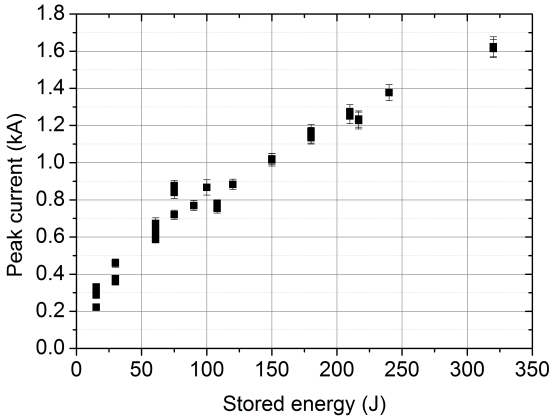

(b)

Figure A.3: The peak current through the plasma during a plasma pulse as a function of stored energy in the capacitors for the pulsed plasma systems in (a) Pilot and (b) Magnum.

Appendix B

Plasma pulses on a dummy resistor

For the characterization of the pulsed plasma system it is necessary to investigate the impedance of the electric components of the system. It was shown in section 3.1 that the changing resistance of the plasma during a pulse makes a study of the impedance of the electronic components difficult. Before the pulsed plasma system was connected to the actual plasma source in Magnum-PSI, the system was tested on a dummy resistor. The resistance of the resistor is 10 mΩ and the inductance is approximately zero. A constant resistance over time does allow for the study of the other electric components of the pulsed plasma system.

It was shown in section 2.2 that during the resonance mode the current increased as

$$I(t) = I_0 \sin(\frac{t}{\sqrt{LC}}) \quad \text{for } 0 < t < \frac{\pi}{2}\sqrt{LC} = \tau_{ramp}. \tag{B.1}$$

If one assumes that the capacitance of the electronic components except for the capacitor, C_{cap}, is zero, one can find the inductance of the wire, L_{wire}, according to

$$L_{wire} = \frac{1}{C_{cap}}(\frac{2\tau_{ramp}}{\pi})^2 - L_{ind} \tag{B.2}$$

where L_{ind} is the inductance of one inductor which is 160 μH. Although $L_{total} = \frac{L_{ind}+L_{wire}}{n}$, this equation is independent of the amount of sections used in a discharge, n. From the dummy analysis the average inductance of the wires as found to be $L_{wire} = 24 \pm 14$ μH.

During the decay mode, the current decays as

$$I(t) = I_0 \exp^{-\frac{R_{tot}t}{L}} \quad \text{for } t > \frac{\pi}{2}\sqrt{LC}. \tag{B.3}$$

If multiple sections are used during a pulse, the total resistance, R_{tot}, can be described as

$$R_{tot} = \frac{R_{wire}}{n} + R_plasma. \tag{B.4}$$

Using this and the total inductance, determined in (B.2), the resistance of the wires can be found according to

$$R_{wire} = \frac{L_{ind} + L_{wire}}{\tau_{decay}} - nR_{plasma}. \tag{B.5}$$

Using the result obtained from the dummy analysis, the resistance found is $R_{wire} = 48 \pm 10$ mΩ.

The time evolution of the power dissipated in the dummy for several stored energies is shown in figure B.1. In the energy scan a single section is used, so the total inductance and total

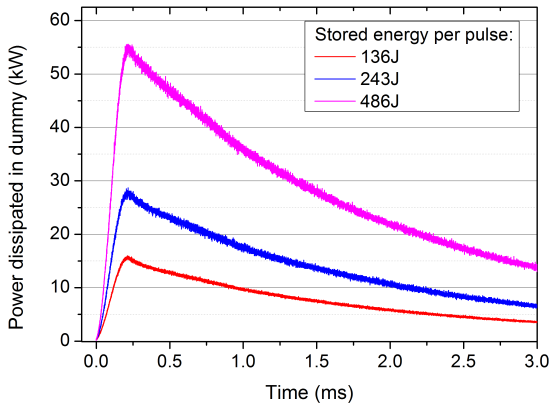

Figure B.1: Power dissipated in the dummy resistor as a function of time. For each pulse one section was used in the discharge.

resistance should be similar. This is indeed observed as both decay time and ramp time are approximately constant. The total decay time is approximately 3.5 ms which is significantly larger that the decay times observed during a pulsed plasma. This is due to the constant and lower resistance of the dummy compared to the variable resistance of the plasma.

The power evolution during a pulse when the amount of sections is varied while the total pulse energy remains constant is shown in figure B.2. Here the decay time does vary significantly which is expected according to equation (B.5). Because the total resistance is increased for a larger number of sections, the peak power does decrease for a larger amount of sections discharged in one pulse. Both effects should be taken into account when varying the amount of sections discharged in one pulse during plasma exposure.

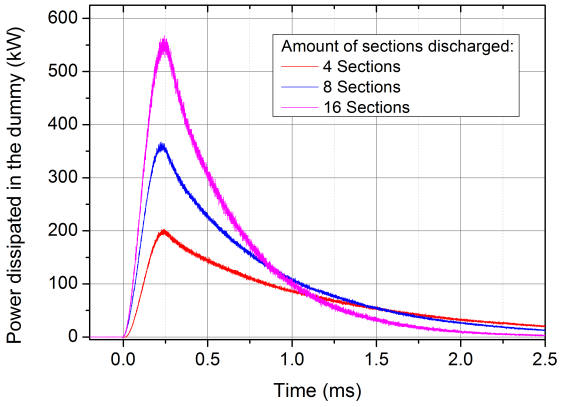

Figure B.2: Power dissipated in the dummy resistor as a function of time. For each pulse a different amount of sections was discharged, while the total stored energy remains constant at 486 J by varying the voltage across the capacitors. Due to the reduced total resistance, the decay time is decreased with a larger number of sections.

Bibliography

[1] D. J. MacKay. *Sustainable energy - without the hot air*. UIT Cambridge, 2009.

[2] J. Freidberg. *Plasma Physics and Fusion Energy*. Cambridge University Press, 2007.

[3] J. Wesson. *Tokamaks*. Oxford : Clarendon Press, 2004.

[4] R. Pitts et al. Status and physics basis of the ITER divertor. *Physica Scripta*, T138, 2009.

[5] ITER.org, facts and figures.

[6] G. Federici. Plasma-material interactions in current tokamaks and their implications for next step fusion reactors. *Nuclear Fusion*, 41, 2001.

[7] G. Janeschitz et al. The ITER divertor concept. *Journal of Nuclear Materials*, 220-222:73–88.

[8] A. Kirschner. Erosion and deposition mechanisms in fusion plasmas. *Transactions of fusion science and technology*, 57:277–292, 2010.

[9] H. Wilson. Edge localized modes in tokamaks. *Transactions of fusion science and technology*, 57:174–182, 2010.

[10] J. Linke. High heat-flux performance of plasma facing meterials and components under service conditions in future fusion reactors. *Transactions of fusion science and technology*, 57:293–302, 2010.

[11] A. Loarte et al. Transient heat loads in current fusion experiments, extrapolation to iter and consequences for its operation. *Phys. Scr.*, T128:222–228, 2007.

[12] M. Mayer et al. Tungsten erosion and redeposition in the all-tungsten divertor of ADSDEX Upgrade. *Physica Scripta*, T138:014039, 2009.

[13] L. Hortona and EFDA-JET Contributors. The jet iter-like wall experiment: First results and lessons for iter. *Fusion Engineering and Desgin*, 2013.

[14] G. van Rooij. Laboratory experiments and devices to study plasma surface interaction. *Transactions of fusion science and technology*, 57:313–319, 2010.

[15] H. Maier et al. Tungsten coatings for the JET ITER-like wall project. *Journal of Nuclear Materials*, 363-365(1246), 2007.

[16] S. Kajita, N. Ohno, S. Takamure, W. Sakaguchi, and D. Nishijima. Plasma-assisted laser ablation of tungsten: Reduction in ablation power threshold due to bursting of holes/bubbles. *Applied Physics Letters*, 91:261501, 2007.

[17] K.R. Umstadter, R. Doerner, and G. Tynan. Effect of bulk temperature on erosion of tungsten plasma-facing components subject to simultaneous deuterium plasma and heat pulses. *Phys. Scr.*, T138(014047), 2009.

[18] I.E. Garkusha et al. The latest results from elm-simulation experiments in plasma accelerators. *Phys. Scr.*, T138(014054), 2009.

[19] K. Umstadter, R. Doerner, and G. Tynan. Enhanced erosion of tungsten plasma-facing components subject to simultaneous heat pulses and deuterium plasma. *Journal of Nuclear Materials*, 386-388:751–755, 2009.

[20] G. De Temmerman, J. Zielinski, S. van Diepen, L. Marot, and M. Price. Elm simulation experiments on pilot-psi using simultaneous high flux plasma and transient heat/particle source. *Nuclear Fusion*, 51:014047, 2011.

[21] J. Zielinski, R. Al, H. van der Meiden, W. Melissen, J. Rapp, and G. De Temmerman. Production and characterization of transient heat and particle pulses in pilot-PSI. *Journal of Nuclear Materials*, 415, 2011.

[22] W.A.J. Vijvers, D.C. Schram, A.E. Shumack, N.J. Lopes Cardozo, J. Rapp, and G.J. van Rooij. Experimental and theoretical determination of the efficiency of a sub-atmospheric flowing high power cascaded arc hydrogen plasma source. *Plasma Sources Sci. Technol.*, 19(065016), 2010.

[23] C.J. Timmermans. *An investigation of pulsed high density plasma.* PhD thesis, Eindhoven University of Technology, 1984.

[24] Jakub J. Zielinski. *A high power pulsed plasma system for materials testing under simultaneous continuous and transient loads.* PhD thesis, Eindhoven University of Technology, 2013.

[25] B. Krijger. Control pulsed plasma source elm simulation. Technical report, Dutch Institute for Fundamental Energy Research, July 2012.

[26] T. Eich, P. Andrew, A. Herrmann, W. Fundamenski, A. loarte, and R.A. Pits. Elm resolved energy distribution studies in the jet mkii gas-box divertor using infra-red thermography. *Plasma Phys. Control. Fusion*, 49:573–604, 2007.

[27] H.J. van der Meiden et al. Advanced thomson scattering system for high-flux linear plasma generator. *Rev. Sci. instrum.*, 83(123505), 2012.

[28] H.J. van der Meiden. *Thomson scattering on low and high temperature plasmas.* PhD thesis, Eindhoven University of Technology, 2011.

[29] A. Herrmann. Limitations for divertor heat flux calculations of fast events in tokamaks. In *28^{th} EPS Conference on Controlled Fusion and Plasma Physics*, 2001.

[30] A. Loarte et al. Progress in the ITER physics basis, chapter 4: Power and particle control. 47(S203-S263).

[31] J.D. Huba. NRL plasma formulary, 2009.

[32] W.A.J. Vijvers et al. Optimization of the output and efficiency of a high power cascaded arc hydrogen plasma source. *Phys. Plasmas*, 15(093507), 2008.

[33] Rob Wiegers. *B2.5-Eunomia simulations of Pilot-PSI.* PhD thesis, Eindhoven University of Technology, 2012.

[34] W. Eckstein. Calculated sputtering, reflection and range values. Technical report, Max-Plank-Institut für Plasmaphysik, 2002.

[35] P.C. Stangeby. *The Plasma Boundary of Magnetic Fusion Devices.* Institute of Physics Publishing, 2000.

[36] A.E. Shumack. *The influence of electric fields and neutral particles on the plasma sheath at ITER divertor conditions.* PhD thesis, Eindhoven University of Technology, 2011.

[37] M.A. van den Berg et al. Thermographic determination of the sheath heat transmission coefficient in a high density plasma.

[38] A. Kreter et al. Nonlinear impact of edge localized modes on carbon erosion in the divertor of the JET tokamak. *Phys. Rev. Lett.*, 4(045007), 2009.

[39] S. Takamura, N. Ohno, D. Nishijima, and S. Kajita. Formation of nanostructured tungsten with arborescent shape due to helium plasma irradiation. *Plasma Fusion Res.*, 1(051), 2006.

[40] G.M. Wright et al. Assessment of tungsten nano-tendril growth in the alcator c-mod divertor. In *IAEA conference*, 2012.

[41] T.W. Morgan et al. ELM-induced melting: assessment of shallow melt layer damage and power handling capability of tungsten in a linear plasma device. In *PFMC conference*, 2013.

[42] J.J. Zielinski et al. Characterization of a high-power/current pulsed magnetized arc discharge. *Plasma Sources Sci. Technol.*, 21(065003), 2012.

[43] H.S. Carslaw and J.C. Jaeger. *Conduction of Heat in Solids.* Oxford Science Publications, second edition edition, 1989.

[44] J. Linke et al. Performance of different tungsten grades under transient thermal loads. *Nuclear Fusion*, 51(073017), 2011.